JGR Space Physics

RESEARCH ARTICLE
10.1029/2024JA032757

Explaining the Evolution of Ion Velocity Distributions at a Low Activity Comet

A. Moeslinger[1,2], H. Gunell[2], H. Nilsson[1,2], S. Fatemi[2], and G. Stenberg Wieser[1,2]

[1]Swedish Institute of Space Physics, Kiruna, Sweden, [2]Department of Physics, Umeå University, Umeå, Sweden

Key Points:

- Hybrid simulations with the Amitis code for a low activity comet show the formation of an asymmetric induced magnetosphere
- The velocity distributions of solar wind protons form partial rings in the simulation as previously reported by observations
- Backtracing the cometary ions in the tail shows that the shape of their velocity distributions is driven by electric field structures

Supporting Information:

Supporting Information may be found in the online version of this article.

Correspondence to:

A. Moeslinger,
anja.moeslinger@irf.se

Citation:

Moeslinger, A., Gunell, H., Nilsson, H., Fatemi, S., & Stenberg Wieser, G. (2024). Explaining the evolution of ion velocity distributions at a low activity comet. *Journal of Geophysical Research: Space Physics*, *129*, e2024JA032757. https://doi.org/10.1029/2024JA032757

Received 16 APR 2024
Accepted 10 SEP 2024

Author Contributions:

Conceptualization: A. Moeslinger
Formal analysis: A. Moeslinger
Funding acquisition: H. Gunell, H. Nilsson, S. Fatemi
Methodology: A. Moeslinger, H. Gunell, S. Fatemi
Project administration: A. Moeslinger
Resources: H. Gunell
Software: A. Moeslinger, H. Gunell, S. Fatemi
Validation: A. Moeslinger
Visualization: A. Moeslinger
Writing – original draft: A. Moeslinger
Writing – review & editing: A. Moeslinger, H. Gunell, H. Nilsson, S. Fatemi, G. Stenberg Wieser

Abstract At a low activity comet the plasma is distributed in an asymmetric way. The hybrid simulation code Amitis is used to look at the spatial evolution of ion velocity distribution functions (VDFs), from the upstream solar wind (SW) to within the comet magnetosphere where the SW is heavily mass-loaded by the cometary plasma. We find that the spatial structures of the ions and fields form a highly asymmetric induced magnetosphere. The VDFs of SW and cometary ions vary drastically for different locations in the comet magnetosphere. The shape of the VDFs differ for different species. The SW protons show high anisotropies that occasionally resemble partial rings, in particular at small cometocentric distances. A second, decoupled, proton population is also found. Solar wind alpha particles show similar anisotropies, although less pronounced and at different spatial scales. The VDFs of cometary ions are mostly determined by the structure of the electric field. We perform supplementary dynamic particle backtracing to understand the flow patterns of SW ions that lead to these anisotropic distributions. This tracing is needed to understand the origin of cometary ions in a given part of the comet magnetosphere. The particle tracing also aids in interpreting observed VDFs and relating them to spatial features in the electric and magnetic fields of the comet environment.

1. Introduction

Comets are known to be one of the most diverse objects in our solar system when it comes to the spatial scales of their magnetospheres (Edberg et al., 2023). This is due to the variability in their outgassing rate, which is a measure of their activity and describes the rate at which the ices near the surface of the comet nucleus sublimate. Because of the small size of comet nuclei, these particles are not gravitationally bound and escape into space. Comet outgassing rates depend on various parameters. To an extent it is an intrinsic quantity individual to each comet since it depends on the nucleus size, surface structure, and nucleus composition. However, it also depends on the heliocentric distance of the comet: comets at their perihelion have outgassing rates that are orders of magnitude higher than when they are several AU away from the sun. The neutral gas profile of a comet is frequently modeled based on the assumption of spherically symmetric outgassing where it follows a $1/r^2$ profile (r: cometocentric distance) (Haser, 1957). This neutral gas gets ionized by photoionization, charge exchange, and electron-impact-ionisation, and creates newborn cometary ions (e.g., Galand et al., 2016). For the solar wind (SW), this cloud of cold ions presents an obstacle: the SW gets mass-loaded (Biermann et al., 1967). The result of this plasma interaction between the SW and the cometary ions depends on the SW parameters as well as the altitude profile of newborn cometary ions. At very low comet activity the SW only gets lightly deflected (Behar et al., 2016; Broiles et al., 2015). At intermediate to high activity the comet magnetosphere may contain several plasma boundaries (Mandt et al., 2016), including a SW ion cavity (Behar et al., 2017; Nilsson et al., 2017) and a bow shock (Neubauer et al., 1986). The comet studied in most detail so far has been comet 67P/Churyumov-Gerasimenko (Taylor et al., 2017), visited by the Rosetta spacecraft (Glassmeier et al., 2007). A review of the observations of the comet plasma environment is found in Goetz et al. (2022).

For intermediate activity at comet 67P the first stage of a bow shock was observed (Gunell et al., 2018) and a magnetosheath formed (Williamson et al., 2022). Regions of heated SW were observed sporadically during low-to-intermediate activity (Goetz et al., 2021). The most detailed study so far of the observed velocity distribution functions (VDFs) at a low-to-intermediate activity comet for a period with very broad SW proton energy spectra revealed that the protons formed partial ring structures in velocity space (Moeslinger, Stenberg Wieser et al., 2023). The ions making up such a partial ring come from many different directions. In an environment small compared to an ion gyroradius these ions may have passed through very different regions of the comet—SW interaction region. Until the Comet Interceptor mission (Jones et al., 2024) delivers the first multi-point measurements of a comet, we have no observations that simultaneously cover different parts of the comet plasma

environment. To fully understand how such ion VDFs form and how we can interpret them, we need to turn to models.

Numerical models of space plasmas can be split into 3 categories: magnetohydrodynamic (MHD) models, hybrid models, and fully kinetic particle-in-cell (PIC) models. Their applicability depends on the spatial scales of the physical processes one is interested in. MHD models are especially suited for studying large-scale objects where both ions and electrons can be considered fully magnetized. Typical subjects of MHD models are plasma interactions between the SW and planets with strong intrinsic magnetic fields, like at Earth and Jupiter. High-activity comets are also modeled with MHD models. Examples include simulations of comet 1P/Halley (Gombosi et al., 1996; Rubin et al., 2014) and comet Hale-Bopp (Gombosi et al., 1997), as well as comet 67P near perihelion (Huang et al., 2016). Fully kinetic PIC models are found on the other end of the scale, where even kinetic effects of electrons play an important role in the physics of the system. However, the computational effort limits the use case to modeling of small-scale objects, for examples comets with very low activity, and small moons (e.g., Phobos). They have been applied to study electron dynamics, such as electron heating and acceleration mechanisms, and electric fields, at comet 67P for large heliocentric distances (>3 AU) (Deca et al., 2017; Divin et al., 2020; Gunell & Goetz, 2023). Hybrid models, like the one used in this paper, are able to fill the gap in between by modeling the kinetic effects of ions. They are typically used to model SW—plasma interactions at objects like low-to-intermediate activity comets Mars (Wang et al., 2023), as well as the Earth's Moon (Holmström et al., 2012). The global comet-solar wind interaction at comet 67P for various outgassing rates and heliocentric distances is frequently modeled using hybrid models (Alho et al., 2021; Gunell et al., 2018; Koenders et al., 2015, 2016).

By studying the VDFs of the plasma species, both in observations and using models, we are able to see the transfer of energy from particles to fields and vice versa. Anisotropic VDFs can be the source of various plasma waves and an indicator for various plasma processes. Examples include pick-up ion distributions (Coates et al., 1989) and ion conics resulting from ion heating and the mirror force (André & Yau, 1997). Kinetic effects are relevant for many processes in space plasmas, in particular at small scales and at boundaries. At a low-outgassing comet, like comet 67P, the environment is continuously changing. The typical scales are smaller than the ion gyroradius, making the environment dominated by kinetic effects. Analyzing the VDFs is necessary to understand the physical processes, both in observations as well as models.

2. Methods

2.1. Hybrid Model Simulations

The core of this study is a hybrid simulation of the comet magnetosphere using Amitis (Fatemi et al., 2017). Amitis is a GPU-based three-dimensional simulation code for space plasmas. The model is well-established and has been applied to various bodies. The results have been verified with spacecraft observations at comet 67P (Gunell et al., 2024), Mars (Wang et al., 2023), Ganymede (Fatemi et al., 2022), and Mercury (Aizawa et al., 2021). It uses the hybrid particle-in-cell (PIC) approximation: ions are modeled as (macro-)particles, while the electrons are modeled as massless fluid. The electron fluid acts as a charge neutralizing background. By treating the ions as particles there is no restriction regarding their distribution in phase space. The ion density ρ_I and the ion current $\mathbf{J}_I$ are obtained from the phase-space distribution of macro particles. The electromagnetic fields $\mathbf{E}$ and $\mathbf{B}$ are computed using the generalized Ohm's law (Equation 1) and Faraday's law (Equation 2). The current density $\mathbf{J}$ is approximated by Ampere's law neglecting the displacement current from $\frac{\partial \mathbf{E}}{\partial t}$ (see Equation 3).

$$\mathbf{E} = -\frac{\mathbf{J}_I \times \mathbf{B}}{\rho_I} + \frac{\mathbf{J} \times \mathbf{B}}{\rho_I} - \frac{\nabla p_e}{\rho_I} + \eta \mathbf{J} \tag{1}$$

$$\frac{\partial \mathbf{B}}{\partial t} = -\nabla \times \mathbf{E} \tag{2}$$

$$\mathbf{J} = \frac{\nabla \times \mathbf{B}}{\mu_0} \tag{3}$$

with $p_e \propto n_i^{\gamma}$, $\gamma = 5/3$, and the vacuum permeability $\mu_0 = 4\pi \times 10^{-7}$ H/m. The resistive term $\eta\mathbf{J}$ in Equation 1 primarily serves to dampen numerical oscillations and does not significantly contribute to the electric fields ($\eta =$

Table 1
Simulation Parameters

	SW H^+	SW He^{2+}	Cometary ions (H_2O^+)
Macro particle weight	1.3×10^{18}	1×10^{17}	1×10^{18}
Upstream speed	430 km/s	430 km/s	–
Upstream density	1 cm^{-3}	0.05 cm^{-3}	–
Upstream temperature (in K)	61.1×10^3 K	214×10^3 K	–
Upstream temperature (in eV)	5.3 eV	9.2 eV	–

5×10^3 Ω m). A more detailed description of the hybrid model equations can be found in Fatemi et al. (2017) and Ledvina et al. (2008).

Table 1 gives an overview of the various simulation parameters. To enable comparison with observations the parameters are based on typical conditions at comet 67P at a heliocentric distance of 2.5−3 AU. The simulation results are stored on a three-dimensional cartesian grid with a spatial resolution of 25 km. Each grid point has a cell of dimensions $(25\ km)^3$ associated with it. The entire simulation space has a size of 7,000 km × 12,000 km × 16,000 km ($x \times y \times z$). In the model reference frame the comet is fixed at (0,0,0). The x-axis points toward the sun ($\mathbf{v}_{SW}$ is along $-x$), and the upstream SW magnetic field is oriented along $+y$, that is, $\mathbf{B} \perp \mathbf{v}_{SW}$, with a strength of 3 nT. The perpendicular field configuration deviates slightly from the expected Parker spiral angle of ≈ 70°, but simplifies the analysis and is not expected to have a strong impact on the simulation results. The time resolution of the simulation is 0.5 ms. We include three different ion species in the simulation: SW protons (H^+), SW alpha particles (He^{2+}), and a cometary ion species with mass 18 amu (H_2O^+). Ions are implemented as so-called macro particles, where one such macro particle represents a fixed number of "real" ions of a certain species. This scaling factor, called macro particle weight, is typically different for the individual ion species. Solar wind ions are injected with a drifting Maxwell-Boltzmann distribution at the upstream boundary, the parameters for both SW species are given in Table 1. The initialized cometary ions are based on a spherically symmetric neutral profile that decreases with radial distance r from the comet (Haser, 1957). Photoionization is the only considered generation mechanism, and the local ion production rate $P(r)$ depends on the comet outgassing rate Q and the photoionization rate $\nu^{h\nu,\mathrm{ioni}}$:

$$P(r) = \frac{Q\nu^{h\nu,\mathrm{ioni}}}{4\pi u_r r^2} \tag{4}$$

with $Q\,\nu^{h\nu,\mathrm{ioni}} = 1.08 \times 10^{20}\ s^{-2}$ (Hansen et al., 2016; Heritier et al., 2018) and the neutral expansion rate $u_r = 700\ m\ s^{-1}$ (Gulkis et al., 2015; Lee et al., 2015). The modeled photoionization rate is about 3–4 times higher than typical at this heliocentric distance to account for the lack of electron-impact-ionisation in our model (Heritier et al., 2017). The cometary macro particles are randomly generated and injected into the simulation at every time step according to this production rate for every grid cell. Increasing the number of particles improves the numerical stability and the statistical properties of the simulation. As a tradeoff, the computational workload also increases. The spatial resolution of the simulation is sufficiently small to resolve proton gyration. Since hybrid models do not require that ions are fully magnetized on the modeled grid scale, we can fully resolve the proton inertial length (227.5 km) without issues.

2.2. Velocity Distribution Functions

The velocity distributions (VDFs) are calculated from the macro particles. Since there is only a small number of particles per cell, the VDFs are integrated in space and time to achieve better statistical properties. Each VDF is calculated for a box of size $(100\ km)^3$ and therefore contains 64 simulation cells. It is desirable not to count the same macro particle many times in a similar volume of the box to ensure that the particles are mostly uncorrelated. For our conditions we can meet this requirement by sampling only every 200th time step. We integrate for a total of 30 k simulation time steps (15 s), which results in a total of 151 individual samples. We note that very slow particles may still be counted multiple times. The macro particles are binned in 3D velocity space. This result is

normalized by macro particle weight (w; different for each species), number of time steps (N_{ts}), box volume (ΔV), and velocity bin volume (ΔV_v):

$$f(\mathbf{x},\mathbf{v}) = \frac{N_{\mathrm{MP}}(\mathbf{x},\mathbf{v})\, w}{\Delta V \Delta V_v N_{ts}} \tag{5}$$

$N_{\mathrm{MP}}(\mathbf{x},\mathbf{v})$ is the number of macro particles in the phase space volume $\Delta V \Delta V_v$ at $(\mathbf{x},\mathbf{v})$. The velocity bin width Δv is identical for all three axes, $\Delta v^3 = \Delta V_v$. It is adjusted for each species based on particle statistics and can be seen in Figure 3. Finally, the result is integrated along the v_y axis, which gives the presented 2D histograms.

2.3. Particle Tracing

The code for the particle tracing (Moeslinger & Gunell, 2024) is an adapted version of the particle tracing code used in Gunell et al. (2015). It uses the electric and magnetic fields from the hybrid simulations to advance the particle positions and velocities for each timestep. The grid size and cell resolution is identical to the Amitis grid. The electric field is corrected by the resistive term to obtain the field $\mathbf{E}_P$ that is applied to the particle motion in the hybrid model: $\mathbf{E}_P = \mathbf{E} - \eta\mathbf{J}$. Since the plasma environment around the comet is highly dynamic, we extended the code to support particle tracing in time-variable fields.

The initial particles for the tracing are directly sampled from the macro particles in the Amitis simulation at a specific time step (here: 300 k). After initializing the fields for the tracing from this time step, they are dynamically updated after each timestep (10 ms) as the simulation progresses. The different ion species are simulated separately. The integration scheme for the particle motion (Boris (1970), see also for example Ledvina et al. (2008)) is symmetric in time, which makes it possible to not only forward- but also backtrace particles, depending on the sign of the tracing time step. In this paper we only used the backtracing capabilities.

3. Results

In this section we give an overview of the simulation results of both the hybrid model and the particle tracing. Both models are fully three-dimensional (see Section 2), and all results are presented in the model reference frame. We will focus on the $x-z$ plane, perpendicular to the upstream magnetic field. The upstream convective electric field in this reference frame is along $+z$, and the $z = 0$-plane divides the space into a $+E$ ($z > 0$) and a $-E$ ($z < 0$) hemisphere. In all figures we show the slice located at $y = 0$, but additional figures for $y \neq 0$ and different projections can be found in the Figures S1 (for the spatial structures) and S2 (for the VDFs) in Supporting Information S1.

3.1. Overview of the Comet Magnetosphere

Figure 1 presents an overview of the comet environment as simulated by Amitis. Panels a–c show the density and projected velocity (i.e., v_x, v_z) of the three ion species included in the simulation (a: Protons, b: Alpha particles, and c: Cometary ions), while panels d and e show the magnetic and electric fields, respectively. All panels show the slice at $y = 0$ (y_0). The y_0-slice is calculated as an average of the two grid layers centered at ±12.5 km. The plasma environment behaves symmetrically around y_0. This symmetry improves the statistical qualities of the shown data without compromising the spatial resolution. At the right edge of each panel (toward $+x$) the plasma approaches its undisturbed upstream state. The results show a highly asymmetric plasma structure with respect to the upstream electric field. The SW ions are deflected toward $-z$, while the cometary ions are accelerated toward $+z/-x$. The magnetic field piles up in front of the comet. A view of the $x-y$ plane at z =0 km is included in the appendix (see Figure A1).

The mean velocities of both SW species are almost completely anti-sunward in the upstream region, with only a slight deflection (Figures 1a and 1b). At x =1,000 km, $z = 0$ the deflection angle between the bulk velocity and the upstream SW velocity is 9.8° for the protons and 6.4° for the alpha particles. Following the flow of the protons (Figure 1a) downstream in the $-E$ hemisphere we note that they are increasingly deflected until they reach a plasma boundary where the density is increased above a factor of 4 with respect to the upstream value. Similar structures have been seen in other simulations, see for example, Gunell et al. (2018) and Koenders et al. (2016, Simulation F), although both simulations model comet 67P at higher activity closer to the Sun. The mean velocity

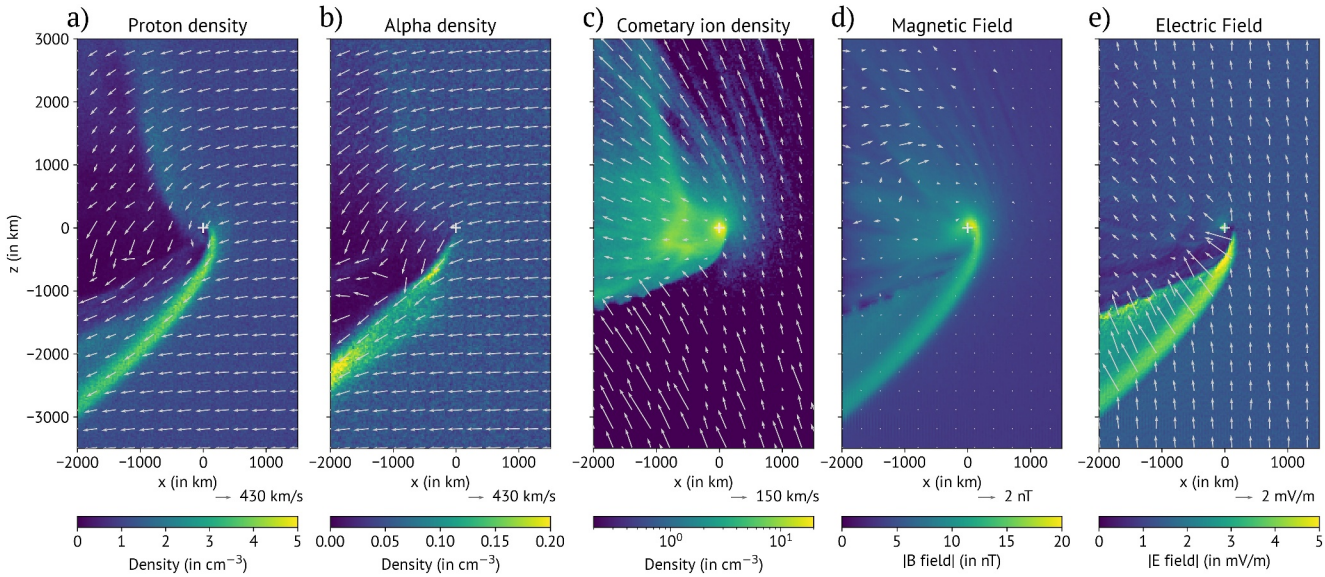

Figure 1. Simulation results in the $x-z$ plane for the slice $y=0$ at timestep 270 k. The comet is located at (0,0,0) (see gray "+" marker), and the Sun is to the right. Panels (a, c) Ion species (a): Protons, (b) Alpha particles, and (c) Cometary ions). The color maps show the ion density. Note that the limits for the different species differ. The arrows show the mean ion velocities ($v_x - v_z$ components only) of the simulation cell at the arrow origin. Panel (d) magnetic field strength (color map; all components) and direction (arrows; $B_x - B_z$ components only). Panel (e) same as panel (d), but for the electric field strength and direction ($E_x - E_z$ only). Arrow length scales are specified above the right side of each color bar.

is along the plasma boundary structure, and no significant deceleration is seen. Far behind the main density enhancement region the protons are depleted. This transition is sharp close to the nucleus and becomes more gradual further downstream. At $x=-1{,}500$ km the density remains elevated by a factor of 3. The nose of the plasma boundary appears at $x=200$ km, $z=-250$ km. In the $+E$ hemisphere the deflection of protons is stronger than in the $-E$ hemisphere, and there is a deceleration of the protons. A transient plasma boundary with a slight density enhancement ($\approx 1.2-1.5$ times the upstream value) can be seen (e.g., $x=-700$ km, $z=500$ km). While the plasma boundary in the $-E$ hemisphere remains stationary, the one in the $+E$ hemisphere slightly varies in position and intensity over time. At the boundary the protons get deflected toward $\pm y$ (out of the plane shown), and the density drops close to 0. The remaining ions in the downstream region have a mean velocity close to or above the upstream SW velocity.

The overall plasma structure of alpha particles (Figure 1b) is similar to that of the protons. Due to the lower number of particles per cell in the simulation compared to the protons the results appear more noisy; this is purely a statistical/numerical effect. In the $-E$ hemisphere the alpha particles are deflected and form a plasma boundary with density enhancements by a factor of $2.5-4$ with respect to the upstream values. The peaks in the density enhancement around $x=-300$ km and $x=-1{,}800$ km are stationary features. The location of the plasma boundary is shifted in the $-x$ direction by a few 100 km with respect to the proton density enhancement. The width is broader than the proton boundary. Downstream of the density enhancement the alpha densities are depleted almost instantly. Comparing the deflection of protons and alpha particles in the $+E$ hemisphere we find that the alpha particles are less strongly deflected, which is in agreement with in situ observations close to the nucleus (Behar et al., 2017). There is no significant deceleration of alphas when moving downstream, and no clear plasma boundary is formed. The depletion due to deflection out of the y_0-plane is more gradual.

The plasma structure of the cometary ions (Figure 1c) is dominated by the imposed newborn ion profile and the electric field structures (shown in Figure 1e). The highest densities occur at the nucleus. In the $+E$ hemisphere the ions are accelerated toward $+z$ along the electric field. At larger distances from the comet the anti-sunward velocity component increases due to a change of the electric field direction and the progressing gyration. Upstream of the nucleus, at $z\approx 0$, the ion density decreases with increasing radial distance from the nucleus, and the ion speed increases. Downstream of the nucleus there is a large region where the density only varies between $3-10$ cm^{-3}. The velocities are mostly anti-sunward, and the speeds increase with radial distance as well. The spatial boundary of this region at smaller z coincides with the upper boundary of the electric field enhancement

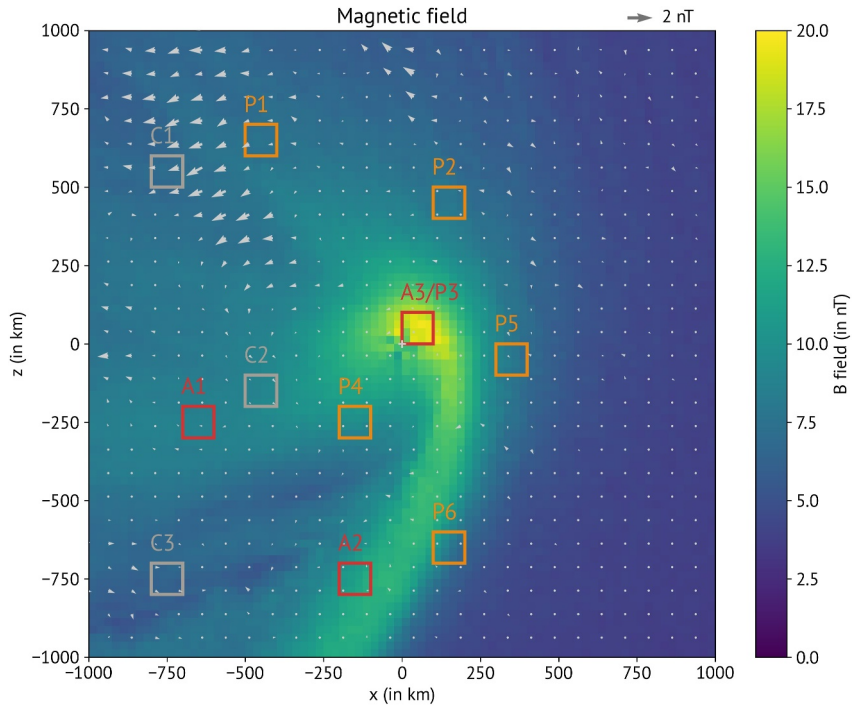

Figure 2. Close-up of the magnetic field at timestep 300 k (background, same quantities as Figure 1, panel d). The boxes show the sampling locations of the velocity distribution functions for the different species; P: protons (orange), A: alpha particles (red), C: cometary ions (gray). Each box has a side length of 100 km and is centered around $y = 0$.

(cf. Figure 1e). At even smaller z values the cometary ion density becomes very small, and the ions behave like pick-up ions in the SW electric field. The mean velocities depend on the exact gyration phase of the sampled particles. At $x \geq 0, z > 1{,}000$ km filament structures appear in the cometary ion density.

Panel d (Figure 1) shows the magnetic field. In the $-E$ hemisphere the increase in magnetic field strength is mostly in the y-direction and the SW ion flow is along the magnetic field enhancement structure. The magnetic field increases up to 15 nT at the nose of the pile-up structure and stays at about 12 nT further away from the nucleus. The pile-up structure coincides with the density enhancement seen in the protons (Figure 1a). The maximum magnetic field strength is 20 nT within 125 km from the nucleus, on the $+x/+z$ side of the comet. A close-up of this region is also shown in Figure 2. Downstream of the nucleus the magnetic field strength drops to about 8 nT within 300 km of the nucleus, and remains relatively constant further tailwards. In the entire $-E$ hemisphere the B_x and B_z components of the magnetic field are negligible. This is not true for the $+E$ hemisphere: wave-like structures appear (similar to Koenders et al., 2016) and B_x and B_z become non-zero. The magnetic field is still enhanced with respect to the upstream value, and varies between 5 and 10 nT. The vortices occurring in the magnetic field (see e. g. at $x = -1{,}800$ km, $z = -1{,}200$ km) are likely numerical artifacts due to the low number of macro particles in this region. The "ripples" parallel to the simulation boundary at $x = -2{,}000$ km are also simulation artifacts. Due to the low amplitude and spatial extent neither are expected to affect the described features in the plasma. They are outside any areas covered in the subsequent analysis.

The electric field (panel e) is mostly dominated by the convective electric field and is also highly asymmetric. In the $-E$ hemisphere it is enhanced due to the pile-up of the magnetic field. The direction remains perpendicular to the flow direction of the SW ions. The maximum electric field strength is above 5 mV/m and is found close to the nucleus (at $x = 0$, $z = -400$ km). This is a factor of 4 larger than the upstream value of 1.3 mV/m. Further away from the nucleus the electric field is still enhanced to 4 mV/m. We define two E-field boundaries for reference in this paragraph: The lower boundary marks the transition between the almost undisturbed upstream SW electric field and the initial E-field enhancement. The upper boundary is toward $+z$ from the lower boundary where the electric field strength drops to values around or below the upstream value. The upper boundary of the enhancement region (at $-1{,}200$ km $\leq z \leq -800$ km) coincides with the drop in the density of cometary ions. In the

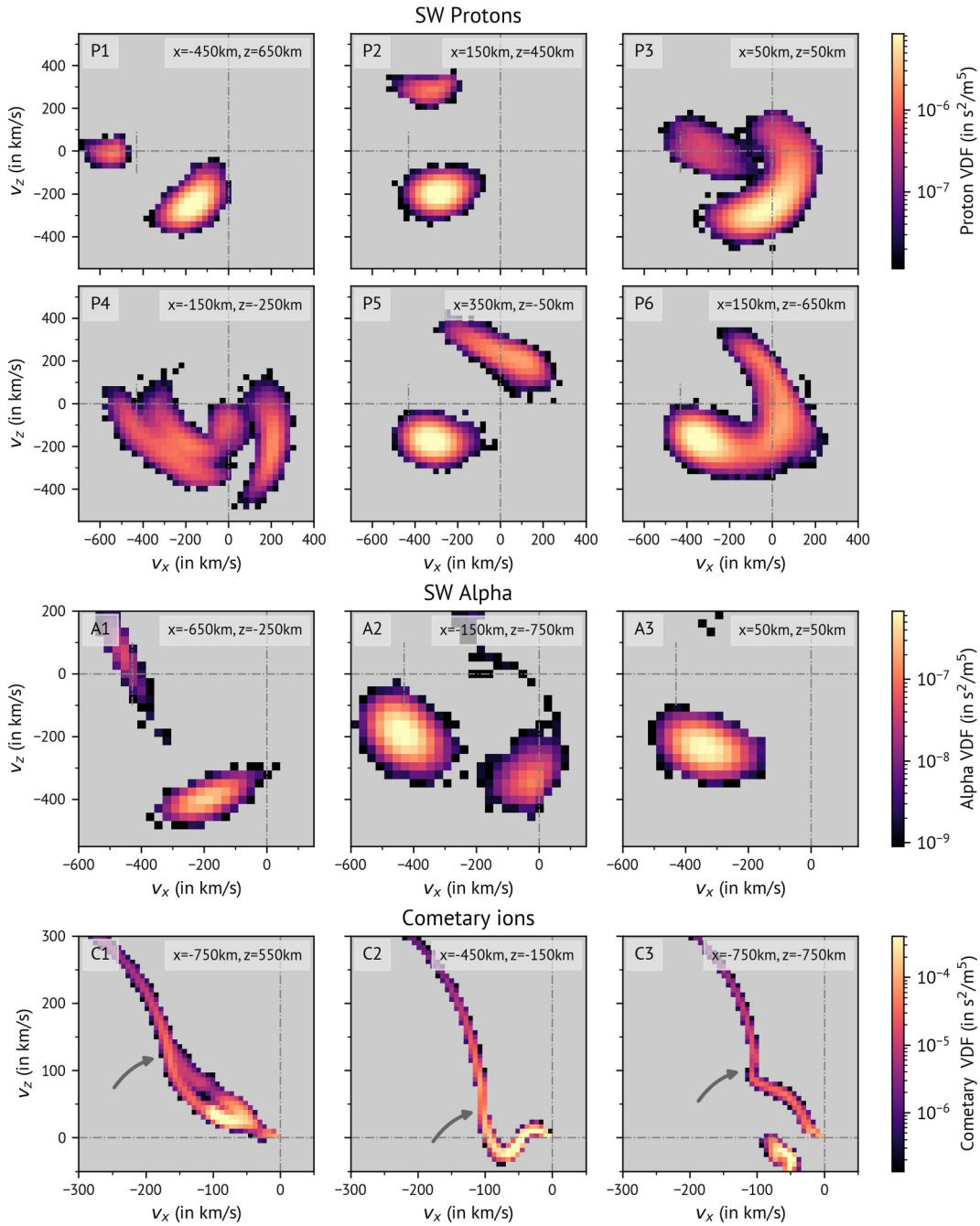

Figure 3. Velocity distribution functions (VDFs) for the locations shown in Figure 2. The box labels and center box locations can be found at the top of each VDF. The VDFs are integrated over the *y*-axis and averaged over the entire box. The dash-dotted lines indicate the velocities $v_x = 0$, $v_z = 0$, and $v_x = 430$ km/s (upstream solar wind (SW) speed; short vertical line, SW species only). For more information see text.

local proton reference frame the electric field at this boundary is pointing in the opposite direction. Its magnitude is about 1 mV/m, with a width of 100 km across the boundary (results obtained via Lorentz transformation using the local proton velocity and magnetic field; see Figure B1). A few 100 km above this boundary, the electric field strength drops to values below the upstream electric field. In the $+E$ hemisphere the electric field is rotated up to 45° around $-y$ at $x < 0$ due to the deflection of SW ions and the flow of cometary ions. There is no enhancement of the electric field strength in this area. Close to the nucleus (<50 km from the center) there is an ambipolar electric field due to the pressure gradient (third term) in Equation 1. This is the only region where the pressure term has

any significant influence. Directly upstream of the nucleus there is a small region that is shielded from the SW electric field. The electric field strength in this shielded region drops to about 0.2 mV/m.

3.2. Velocity Distribution Functions

For evaluating the VDFs we identified different regions of the magnetosphere. Figure 2 shows a close-up of the magnetic field where the different regions can be seen. Within each region the VDFs continuously evolve. The presented VDFs should thus be seen as a typical example for the region and will not be identical away from the sampling location. All sampling locations for each species are labeled and indicated with boxes in Figure 2. Figure C1 shows the sampling locations of each species with respect to their ion density profile.

Proton VDFs are calculated at six different locations, P1–P6. In the $+E$ hemisphere P1 samples the downstream ($x < 0$) region while P2 samples the upstream ($x > 0$) region. P3 is located in the area of maximum magnetic field pile-up close to the nucleus. This region can also be compared to observational results. In the $-E$ hemisphere one sampling point is located in the region downstream of the magnetic pile-up boundary (P4). P5 is upstream of the nose of the proton density enhancement, while P6 samples the region right at the proton density enhancement. The VDFs of the alpha particles are obtained in the downstream region (A1) and the alpha density enhancement (A2). A2 is slightly offset toward $-x$ compared to P6 due to the shift in spatial structures between the protons and alpha particles. A3 is in the same area as P3, for comparison with observations. The alpha particle VDFs in the remaining $+E$ hemisphere are almost Maxwellian, therefore no additional results are shown. Cometary ion VDFs are only analyzed in the downstream region at three different locations. The samples are taken at sufficient distance from the nucleus so that the observed cometary ion velocity distributions had time to evolve. A continuous sampling of VDFs from $x \in [-800$ km, 800 km] and $z \in [-800$ km, 800 km] for $y = 0$ km, $y = -300$ km, and $y = -600$ km for all three species can be found in the in Supporting Information S1. This includes the upstream region of only slightly deflected, Maxwellian-shaped SW.

Figure 3 shows the calculated VDFs for the highlighted sampling locations. The box labels and box center locations are given at the top of each VDF. The lowest value on the color bar represents the occurrence of exactly one macro particle in the calculation of the VDF. It can help to get a statistical estimate of the likelihood of occurrence, i. e., bins with such low values are not statistically significant. However, those with a VDF one-two orders of magnitude higher are.

In panel P1 (top left) two distinct proton populations can be identified. The main population (that with highest phase space density) is highly deflected compared to the upstream SW. Its shape is slightly anisotropic compared to a perfect Maxwellian distribution. The second population has a much lower phase space density and an anti-sunward velocity of about $v_x \approx 550$ km/s. The main population at P2 is less deflected, and the secondary population has a slightly higher phase space density and a significant flow component in the z-direction. Close to the nucleus (P3) the main population forms a partial ring. The deflection from the upstream SW direction ranges from 45° to up to above 270°, although the phase space density decreases for very high deflection angles. A secondary population moving roughly in the anti-sunward direction is also observed. The velocity spread of the secondary population here is quite large, and its speed is typically below the upstream SW speed. Upstream the nose of the proton density enhancement (P5) the main population is a slightly deflected Maxwellian distribution with a mean velocity slightly lower than the upstream SW velocity. The secondary population has a much broader velocity distribution and the mean velocity is directed in the opposite direction. At sampling location P6 (right at the proton plasma boundary) the distribution is similar to P5. However, the secondary population is much broader, and the two populations begin to merge. The VDF calculated at P4, downstream of the boundary, shows four distinct populations. All four populations have much lower phase space densities than any of the main populations observed in the other sampling locations.

There are two alpha particle populations in the region downstream of the alpha density enhancement (Panel A1, third row of Figure 3). Their VDFs have a non-Maxwellian shape. The phase space density of both populations is much lower than the upstream SW alpha particle density (compare to Panel A3). At the alpha particle density enhancement A2 a slightly deflected main population is seen. Its mean speed of 442.7 km/s exceeds the upstream SW speed. The secondary population is deflected by 90°, which is less than the protons in the comparable VDF (P6). Both populations still have a roughly Maxwellian shape. There is a 3rd population at positive v_z, but due to low counts we do not expect it to be a permanent feature of the VDF in this region. Sampling the VDF close to the nucleus (A3) we only observe one population. It is deflected by about 30° and slightly anisotropic.

The bottom row of Figure 3 shows the VDFs of the cometary ions. A radially expanding population is only observed within 100 km of the nucleus (data not shown). All three sampled VDFs (C1–C3) have a high-velocity component that appears circular. It starts at $v_x = -180$ km/s, $v_z = 100$ km/s for C1, at $v_x = -100$ km/s, $v_z = 0$ for C2, and at $v_x = -120$ km/s, $v_z = 80$ km/s for C3, as indicated with arrows. For velocities below these values, the VDFs are intricately shaped but different for all three cases. None of them resembles a Maxwellian distribution. Only at C3 we see two distinct low-velocity populations: one connected to the higher velocity part with positive v_z, and another one with higher intensity and less velocity spread at negative v_z. At C1 and C2 the different parts of the VDF are all connected. Whether these VDFs are comprised of different overlapping populations cannot be said from this plot.

3.3. Particle Tracing

We selected some of the VDFs presented in the previous section for the particle back-tracing: P1, P3, P5, A2, and all cometary VDFs (C1, C2, C3). The main goal is to identify differences in the ion flow patterns for the different parts of the VDF. From the different individual trajectories we assess what regions in the magnetosphere they pass through. With the SW particles one main point is to identify the upstream regions where the particles originated. This also gives the associated upstream VDF of these particles, which is a subset of the Maxwellian-shaped VDF of the upstream SW. For the cometary ions it helps to understand where the particles that make up different parts of the VDF were born.

3.3.1. Solar Wind Ions

Tracing results for both SW species are presented in the same format for all chosen sampling locations (Figures 4–7). Panel a shows a density map of the trajectories of all ions back-traced from the sampling location (see boxes defined in Figure 2). The ions are sampled at a single Amitis time step (at $t = 300$ k). The density is summed over the entire y-axis. Upstream at $x = 4{,}000$ km the velocities of the ions are measured at different z locations by cubic probes. The probes are separated by 250 km along the z axis and their locations are indicated by the black boxes. The probes are labeled in descending order, i. e., the top probe is probe 1. Panel b shows the VDFs for all probe locations. It should be noted that the measured ions in each probe only show what part of the upstream SW population can reach the tracing origin. The complete distribution at this point is a 3D Maxwellian, as defined in the simulation parameters for the hybrid model. Since the relation of the tracing and probe densities to typical physical quantities are rather unimportant, they are not normalized and presented only in arbitrary units. Panel c shows the trajectories of several individual particles. The line colors refer to the different observed velocities at the starting position. The initial velocity for each particle is seen in panel d, on top of the time-averaged VDF at this observation point (same as shown in Figure 3).

Figure 4 shows the back-tracing results of observation point P3 (protons; close to the nucleus). The major part of all particles enters the observation region after a deflection of about 90° from the upstream SW flow and only passes through the $+E$ hemisphere. A smaller portion shows more evolved flow patterns and is observed after completing a full gyration loop (see panels a and c). All traced particles originate within 1,500 km along the z-axis at the probe location. The majority of the particles are back-traced to within 1,000 km and are observed in Probes 4 and 5. The VDFs of the individual probes (Panel b) are similar for all probes: they have a spread of about 100 km/s along v_z, centered at $v_z = 0$. The spread in the v_x direction is only about 50 km/s for an individual probe. Its mean ranges from $v_x \approx -490$ km/s at probe 2 to $v_x \approx -360$ km/s at probe 7. Probes 4 and 5 have mean v_x velocities at about the SW speed. Exceptions from this elongated main cluster occur at higher v_x. For the main population there is a correlation between observed velocity and upstream origin along z (panels c and d). Particles with lower energy and higher deflection originate from larger z compared to their higher energetic, less deflected counterparts. The gyration pattern of the particles belonging to the secondary population is especially clear in panel c (blue trajectories, for initial velocities see panel d). They are reflected right at the nose of the proton density enhancement region. The upstream origin of these particles is the same as the peak of the main population.

Figure 5 shows the back-tracing results of observation point P1 (protons; downstream in the $+E$ hemisphere). Two distinct flow patterns are seen. The upstream origin of the main population at the probe location is within about 1,500 km along the z-axis, with the major part originating within 500 km (see panels a and c). The correlation between observed velocity (energy) and reconstructed origin along z is similar to what is seen at P3 (Figure 4). All particles of this population are at an initial stage of gyration. The secondary population originates

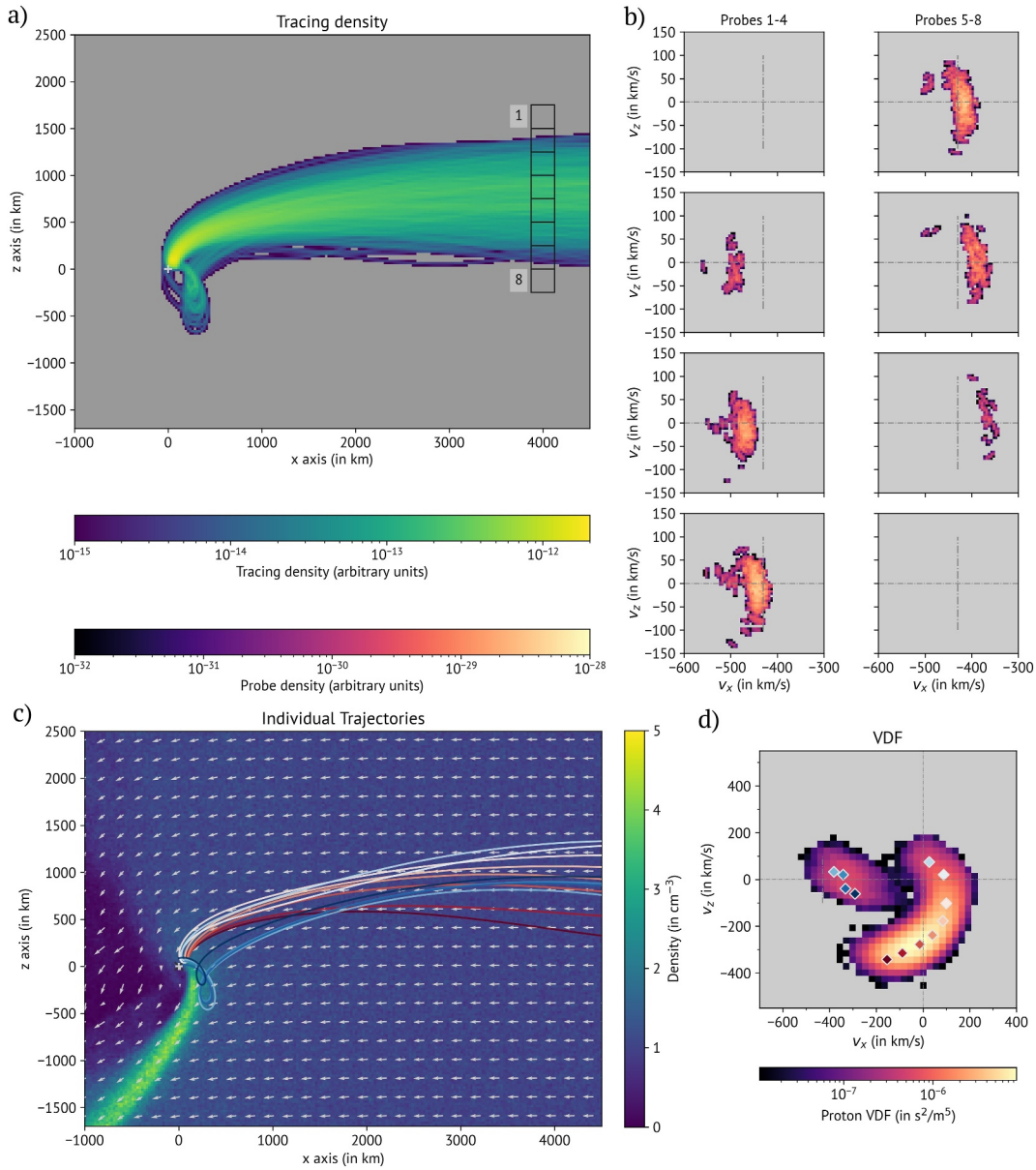

Figure 4. Particle tracing results of box P3 (protons), initial Amitis time step: 300 k. Panel (a) Density map of all initial particles in the $x-z$ plane, integrated over the entire y-axis. The boxes around $x = 4{,}000$ km mark probe locations for the back tracing velocity distribution functions (VDFs) (see panel b). The probes are labeled by descending z-coordinate, with probe 1 at the top. Panel (b) VDFs of the back-traced particles for different probe locations (see panel a). Only the particles that pass through P3 are included; the complete VDF at this point is Maxwellian. The dash-dotted lines indicate the mean upstream solar wind velocity. Panel (c) Background: proton density and mean velocity. Overlay: Individual trajectories of selected particles. The corresponding initial velocity for each particle is shown in panel (d) (indicated by marker/line colors).

from smaller z-values. The particles have completed a full gyration from the upstream to the observation point and pass through the upstream region close to the nucleus. Probes 2–5 (panel b) contain most of the back-traced particles of the main population. The shape of the distribution is similar to that of the main population at P3 (Figure 4). The upstream VDF of the secondary population is mostly captured by probe 6, but parts of the distribution are seen in probes 5 and 7.

Sampling location P5, upstream of the proton density enhancement structure, is shown in Figure 6. The main population appears only deflected, while the secondary population shows significant gyration. Contrary to the previous two figures, the secondary population originates from larger z-values compared to the main population.

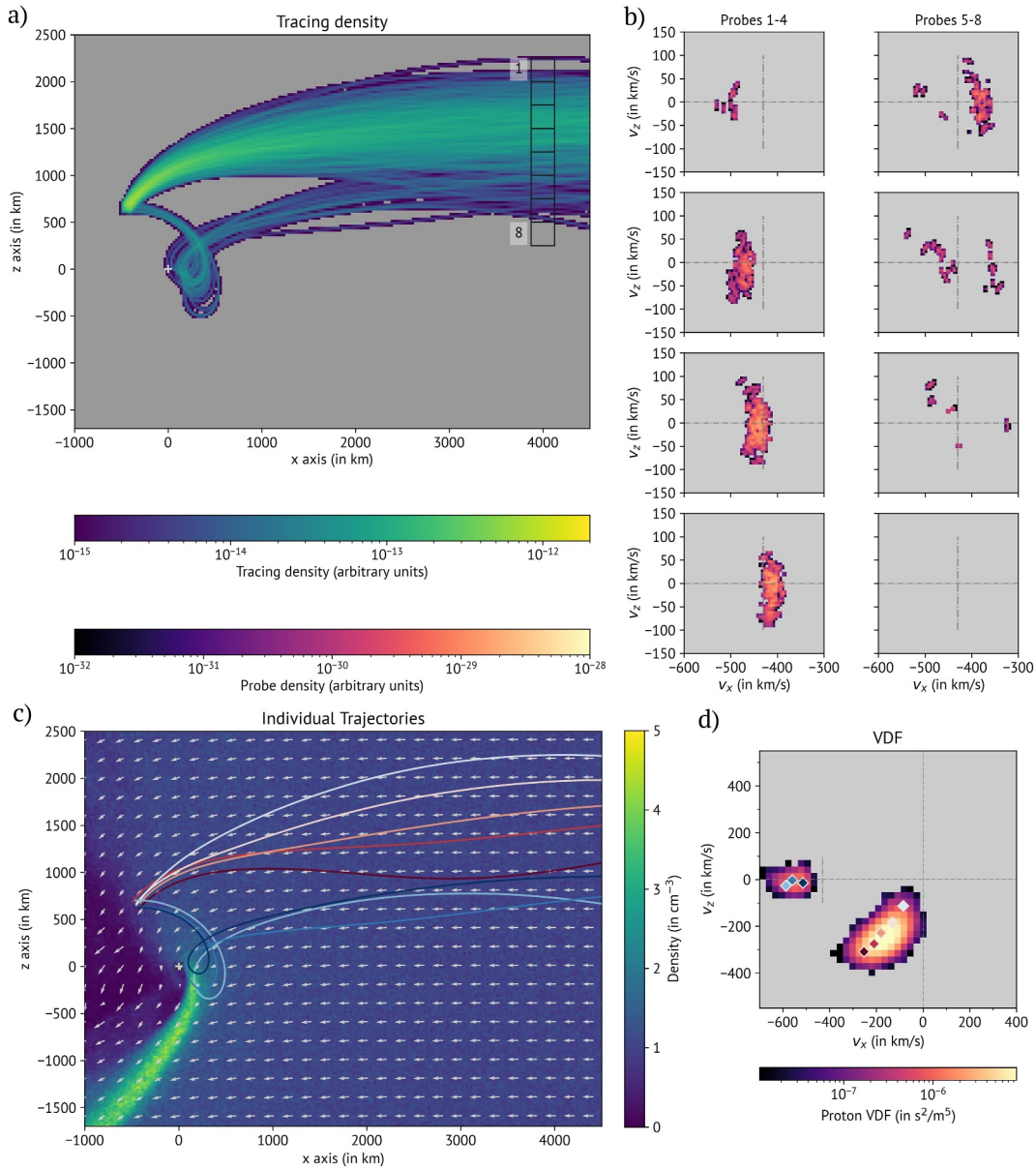

Figure 5. Particle tracing results of P1 (protons). For panel description see Figure 4.

Probe 3 shows a broad distribution of observed velocities, which is probably due to a mixture of both populations. The major axis of the elongated distributions in probes 4–7 are not vertical but are rotated by about 20°.

Figure 7 shows the back-tracing results of the alpha particles at A2 (the alpha particle density enhancement region). The overall structure is comparable to the protons at P5 and P6 (Figure 6). The two different populations separate by their upstream origin. The secondary population originates from larger z in the $+E$ hemisphere. The upstream VDFs of the main population (Panel b, probes 4–8) are rotated about 50° from the vertical axis, which is even more than the protons at P5. Apart from the rotation the alpha VDFs are similar to the SW protons. The individual probe VDFs appear shifted perpendicular to their major axis toward $+v_x/+v_z$ for decreasing z.

3.3.2. Cometary Ions

For the cometary ions we compiled all three sampling locations (C1–C3) into one figure (see Figure 8). The top row shows the back-tracing trajectories, and the bottom row shows the corresponding initial velocities for the

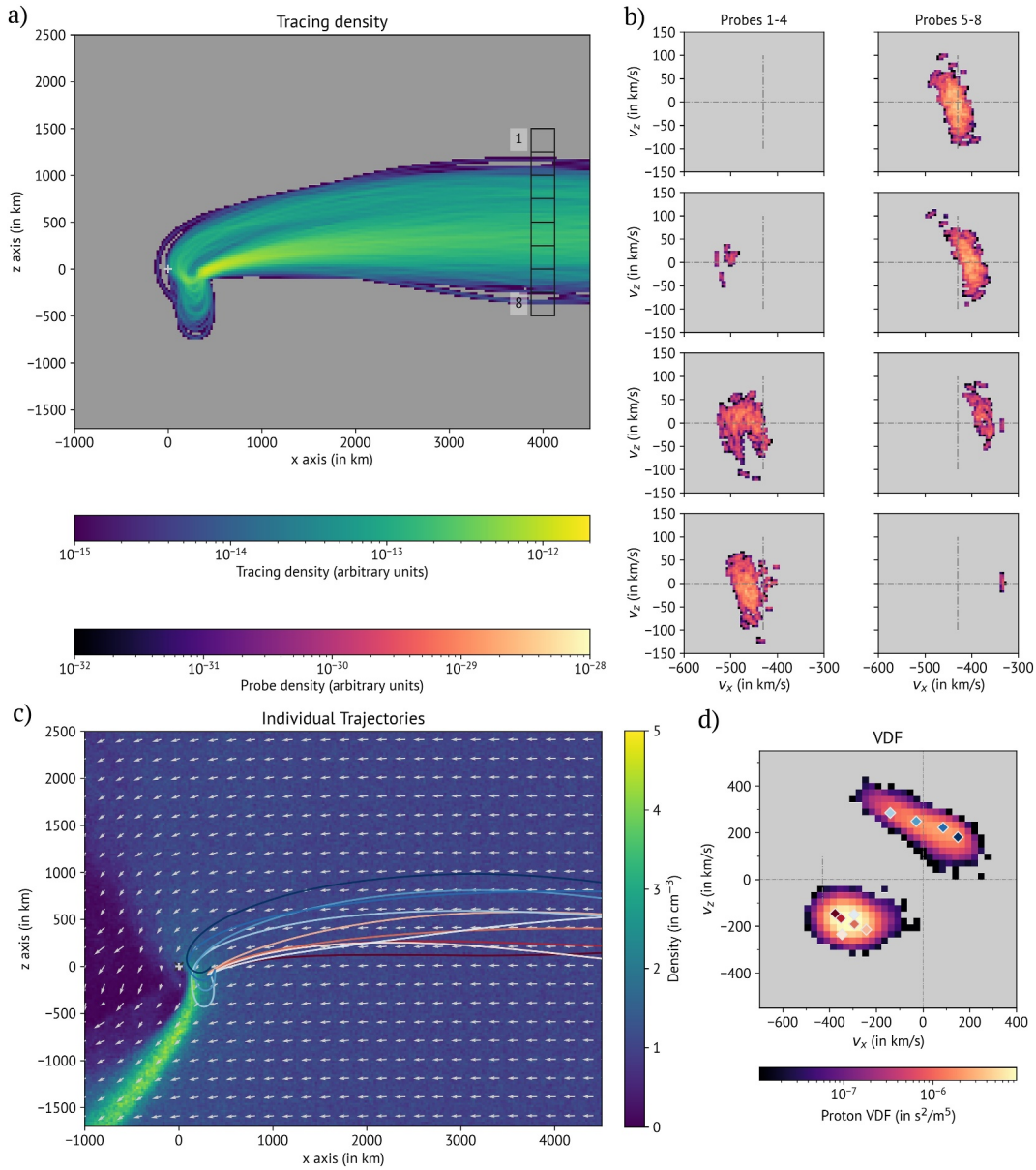

Figure 6. Particle tracing results of P5 (protons). For panel description see Figure 4.

illustrated trajectories. The columns show C1 (left), C2 (middle), and C3 (right), respectively. The electric field in the background of the top panels is the initial electric field that is used for the particle tracing; it does not include the resistive term (η**J**) from the hybrid model. The termination point of the particle trajectories is the location where the particle had its lowest energy during back-tracing. This should roughly correspond to the location where they are born. We note that the cometary ions born outside the y_0 plane are in general deflected toward y_0, which is opposite to the flow of SW particles. The back-tracing is done using time-variable fields. This means that the electric field affecting the newborn particles may be different to what is shown in Figure 8.

At sampling point C1 (left column) particles with speeds up to 120 km/s are predominantly driven by the structure of the electric field. The two different branches visible in the VDF relate two slightly different groups of trajectories. Above 120 km/s the gyration pattern of the ions becomes more important (see light blue trajectory). At C2 (middle column) the trajectories can be split up in three different groups. Ions up to 70 km/s originate from the region with low electric field strength downstream of the nucleus. Particles with velocities above 100 km/s originate in the undisturbed SW and show the typical pickup-ion distribution. They are further accelerated by the

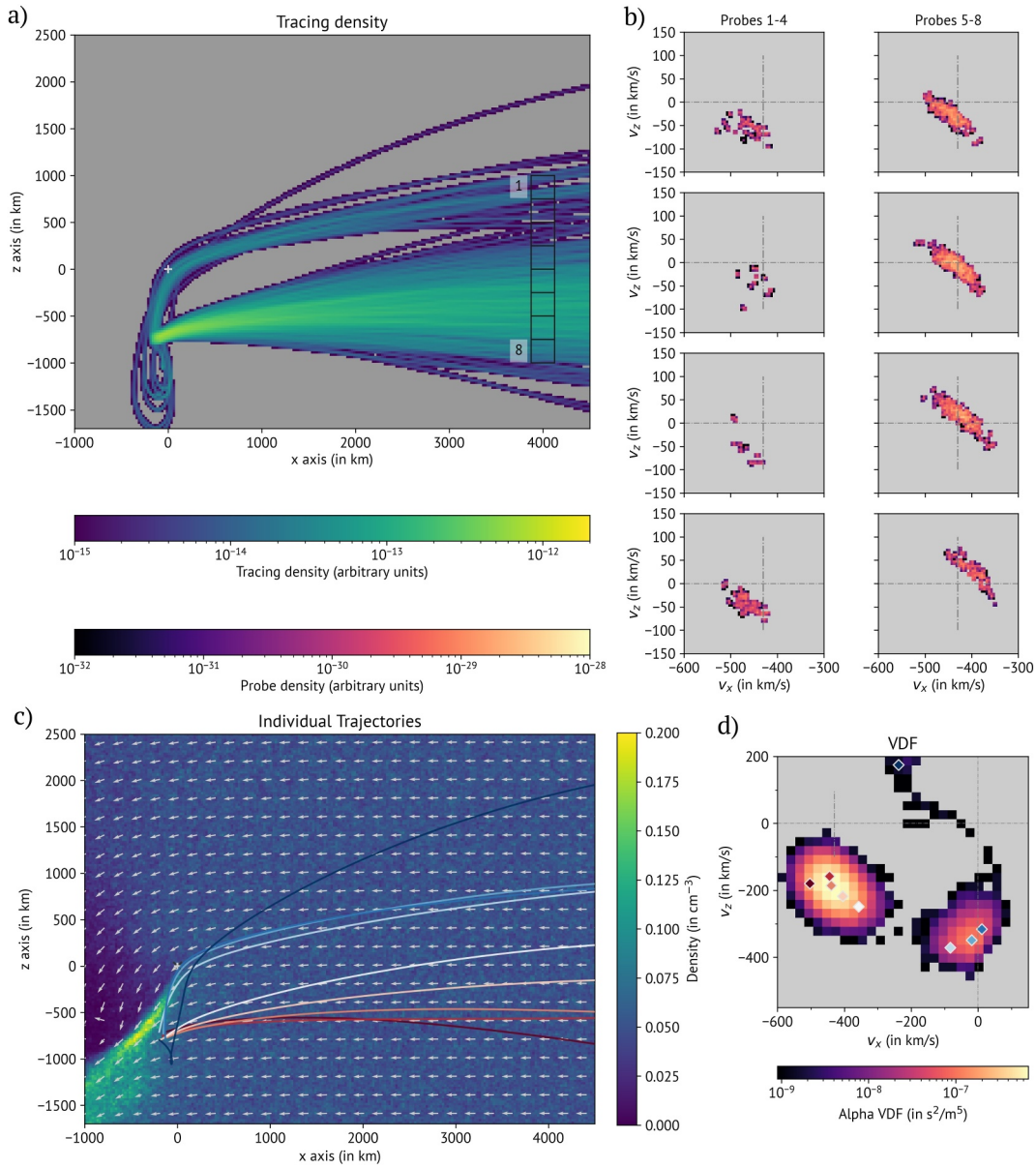

Figure 7. Particle tracing results of A2 (alpha particles). For panel description see Figure 4. Panel (c), background: alpha particle density and mean velocity.

electric field enhancement region they pass through. In the velocity range between 70 and 100 km/s the ions originate from upstream the nucleus but do not directly pass through the electric field enhancement region. The back-traced trajectories from C3 (right column) show two distinct groups of trajectories for the two distinct populations in the VDF. Ions with initial velocities $v_z > 0$ all come from the $-z$ direction. The transition between the two different circular arcs of the VDF seems to coincide with the ions originating from the undisturbed SW (higher velocities) or the electric field enhancement region (lower velocities). The arc below $v_z \approx 100$ km/s appears to result from the electric field in the enhancement region, not from a partially developed gyration of the particles. The second population $(v_z < 0)$ originates from a completely different region, close to the nucleus.

4. Discussion

For the discussion we will retain the distinction between the $+E$ (for $z > 0$) and the $-E$ (for $z < 0$) hemispheres, but since this definition is based on the upstream parameters of the plasma, it is not sufficient to cover all observed

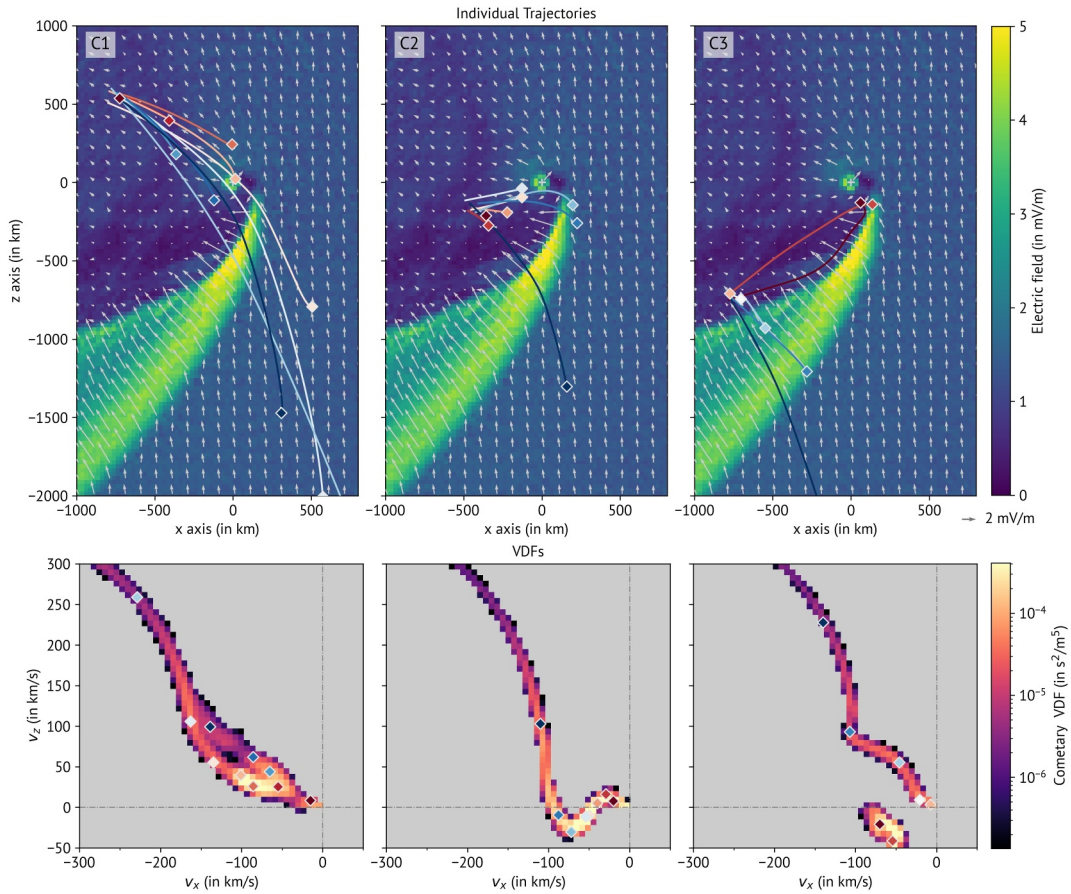

Figure 8. Particle tracing results of cometary ions (C1–C3), projected onto the $x-z$ plane. Upper row: Background: electric field strength and direction ($E_x - E_z$ only) at $y = 0$ used for the particle tracing. Overlaid: Individual particle trajectories from the three box origins C1–C3 (from left to right). The trajectories are terminated at the lowest velocity point ($v \approx 0$). Lower row: Velocity distribution functions and corresponding initial particle velocities for the three box locations C1–C3.

features. We therefore introduce a third region, the "central tail," which is the region where the cometary plasma dominates. This roughly spans the area from the nucleus toward $-x$ within a 35° cone. The SW ions in this region have retained none of their upstream parameters and the density is heavily depleted.

The plasma in the y_0 plane forms an asymmetric induced magnetosphere. In the $-E$ hemisphere an obstacle similar to a planetary bow shock is formed: a steep increase in the magnetic field strength and an enhancement of the SW density along with its deflection around the obstacle. Upstream of the boundary we observe protons that have been reflected from the boundary. Similar reflected SW ions have been reported at Mars' bow shock (Madanian et al., 2020) as well as Earth's bow shock (Graham et al., 2024; Sckopke et al., 1983). The electric field in the proton reference frame is directed outwards, away from the obstacle toward $+x/-z$. The $+E$ hemisphere provides one of the two main escape paths for cometary ions. This corresponds to the typical pickup-ions observed at comets at all activity levels (e.g., comet 67P (Berčič et al., 2018), and comet 1P/Halley (Neugebauer et al., 1989):), but also at planets with induced magnetospheres (Mars (Dong et al., 2015), Venus (Dubinin et al., 2013):) as well as Mercury (Jasinski et al., 2020; Sun et al., 2024). SW protons may enter the central tail region via this path. The second escape path for cometary ions is via the central tail. The $+E$ hemisphere is more susceptible to wave generation compared to the $-E$ hemisphere.

4.1. Spatial Structure

The asymmetry between the $+E$ and the $-E$ hemispheres is seen both in particle and in field data. The proton and alpha density enhancements are created by the deflection of SW particles toward $-z$. Such an asymmetric

structure relative to the upstream electric field is typical for structures on a spatial scale smaller than an ion gyro radius, such as comet 67P at large heliospheric distances. Newborn cometary ions are accelerated along the electric field. To conserve momentum along the electric field direction (orthogonal to the SW drift direction) the SW particles must be deflected against the electric field. This is also consistent with the cometary ions gaining energy and the SW ions losing energy. In the magnetic field reference frame this can be seen as the total plasma (magnetic field) slowing down due to mass loading and the SW ions now having a motion relative to the magnetic field and thus starting to gyrate. In the comet reference frame this first part of the gyration is a motion against the electric field. In our simulation the proton and alpha particle densities form a clear plasma boundary in the $-E$ hemisphere due to this deflection. The focusing of the flow lines is the primary cause for the sudden increase of the SW densities, since there is no significant deceleration of the flow as it approaches the boundary. Even though the Alfvén speed increases in the proton enhancement region due to the increased magnetic field strength, the SW remains super-alfvénic throughout the simulation.

We can compare the relative enhancement of the proton density (≈ 4 times) and the magnetic field strength ($\approx 4-5$ times) with respect to the upstream plasma. The similar values indicate that the flow line compression and corresponding increase in density is the main driving factor behind the magnetic field pile-up in this region. The electric field structure in this region is still dominated by the convective electric field of the SW protons. Its increase in strength is due to the increased magnetic field strength, while the change in direction results from the deflection of the SW protons. The width of the proton density enhancement region (about 200 km across the boundary where the relative density increase is at least a factor of 3.5) is the result of the deflection geometry and the local velocity distribution. The deflection is spread out over a large spatial scale due to the finite gyroradius of the ions, which puts a lower limit on the width of this boundary. Additionally, the protons have a significant spread in velocity (see e. g. Figure 3; Panel P6). A perpendicular speed of just 50 km/s relative to the bulk flow in the boundary corresponds to a gyroradius of 35 km perpendicular to the boundary. Toward $-x$ downstream of the peak proton density the protons do not disappear completely, despite their mean velocities being directed parallel to the boundary. Those protons may be of different origins.

1. Protons that diffuse through the boundary. These may either be protons with higher velocities than the bulk SW proton flow, or those that have previously been reflected at the boundary and have now gained sufficient energy to pass through.
2. Protons entering through the $+E$ hemisphere. The majority of this flow is deflected out of the y_0 plane, so what remains are tails of the bulk population.

A more in-depth discussion of this can be found in Sections 4.2 and 4.3 which discuss the details of the VDFs and the particle tracing.

The shift of the location of the alpha density enhancement toward $-x$ (and to a lesser extent $-z$) can be explained by the higher inertia (higher m/q) of the alpha particles. The peaks in the alpha density enhancement appear to be focus points of the alpha particle trajectories. The gyroradii of the alpha particles are larger than the proton gyroradii, and there is less deflection in the flow of alpha particles. This creates a difference between the mean velocities of protons and alpha particles, and the corresponding reference frames differ. In the local reference frame of the alpha particles there is an electric field over the proton density enhancement region which accelerates the alpha particles instead of decelerating them. There is an energy transfer from the SW protons to the alpha particles in this region, and the alpha particles create an obstacle to the protons due to their difference in gyroradius. This effect is only relevant if the spatial scales of the boundaries are similar to the gyroradii of the SW species. The consequences of different alpha/proton ratios on the boundary formation in such a case are difficult to predict but should be investigated further in the future.

No clear plasma boundaries are visible in the $+E$ hemisphere. The changes in the plasma environment are more gradual. There is no visible focusing of the SW protons or alpha particles in the y_0 plane. A stationary focusing of protons or alphas into the y_0 plane is highly unlikely since there is no force pushing the SW ions back toward y_0. Thus, any density enhancement must be due to a local deceleration of the mean particle flow, or the result of asymmetries along the y-axis.

Close to the nucleus at $+x/+z$ the increase in magnetic field strength is a result of the deceleration of the SW, and the addition of mass in form of cold, newborn cometary ions. This in turn decelerates the local electron fluid and

results in the magnetic field pile-up in this region. Further away from the nucleus in the $+E$ hemisphere the magnetic field remains enhanced because the plasma is more and more dominated by the cometary plasma. The magnetic field transitions from being frozen into the SW plasma to being frozen into the cometary plasma, and the flow of cometary ions increasingly shapes the structure of the magnetic and electric field.

In general the $+E$ hemisphere shows much more variation of the plasma structures in time and space. We interpret this as the result of wave activity. This affects the magnetic field, the protons (especially in the density), and the cometary ions (data not shown). For the alpha particles the spatial scales in this simulation are probably too small to allow for the development of wave activity. The shielded region directly upstream of the nucleus may be formed by a polarisation electric field that partially cancels the SW electric field, as proposed by Nilsson et al. (2018). By analyzing the VDFs of accelerated cometary ions in this region, Moeslinger, Nilsson et al. (2023) reported an average electric field strength of 0.21 mV/m, very similar to the minimum values found in our simulations.

4.2. VDFs

Comparing the VDFs of any of the three species at any location within the comet magnetosphere (Figure 3) with their mean velocity counterparts (Figures 1a–1c) shows just how much information is lost when only considering the latter. We use the VDFs to study deviations from a Maxwellian in the bulk populations and identify secondary populations. While the details of the particle trajectories are discussed in Section 4.3 below we emphasize that the evolution of VDFs is due to the particle trajectories. In both SW species we never see a formation of a gyrotropic plasma. This is because all structures in the magnetosphere that strongly influence the particle motion are smaller than or of the same size as the particle gyroradius. While there is gyration of each particle that has non-zero velocity in the upstream SW reference frame, we only consider gyration that occurs due to the interaction with the comet. In this context we use the word deflection to describe small angular changes ($<90°$) in velocity, while gyration refers to large angular changes in velocity and the corresponding cycloid trajectories. Angular changes are defined as the angle between the upstream SW direction ($\mathbf{v} = (-430,0,0)$ km/s) and the observed bulk velocity of the ion species, where 0° indicates no deflection.

The majority of protons in the $+E$ hemisphere are significantly decelerated, along with their deflection toward $-E$, and most of the cometary ions are accelerated along the electric field. The main source of free energy to support acceleration are the local SW protons. In theory, other regions could also provide energy to the cometary ions by wave-particle-interaction (e.g., Alfvén waves). But those mechanisms are much less effective in transporting energy and are therefore not expected to significantly contribute to the energy budget. Further into the coma (toward $-x$, compare P2 to P1) the deflection and deceleration increases as the protons are more and more influenced by the cometary ions. A minor part of the protons in the $+E$ hemisphere, seen as a secondary population, are actually accelerated. They must gain energy while passing through the region with strong electric fields and gradients close to the nucleus, not following the bulk flow of protons. Once they have reached the fairly homogenous $+E$ hemisphere further downstream of the nucleus they are gyrating in the local fields. Other than their variation in energy due to this gyration motion, they will only lose energy via wave-particle interaction. This is expected to only be relevant multiple full gyrations far downstream in the tail.

In the $-E$ hemisphere protons are not significantly decelerated, only deflected (P5 and P6). They create the plasma structures in this part of the comet magnetosphere, but are not providing much energy to the cometary ions. Some of their energy, however, must go into building up the plasma structures in this region. Secondary populations are typically first seen close to the nucleus or in the $-E$ hemisphere, where they resemble ions reflected from a shock. They are therefore often observed as counter-streaming the main SW flow. Depending on their exact origin, they may enter the $+E$ hemisphere as their gyration progresses. Especially for these particles there is no obstacle in form of an electric field that they have to climb. Hence they retain some of the energy they gained during the gyration and are now faster than the upstream SW. The ions that do not enter the $+E$ hemisphere still gain enough energy to pass over the proton density enhancement.

The most anisotropic proton population, resembling a partial ring, is seen close to the nucleus (P3). This is the region where we have the strongest magnetic and electric fields, but also the strongest gradients in those fields. The secondary population must be generated in a similar way as in all other cases: it consists of a small portion of the upstream SW that has already performed a full gyration when arriving at the sampling location. Partial ring

distributions have been observed by Rosetta in a few cases (Moeslinger, Stenberg Wieser et al., 2023). However, the model results indicate that these partial ring-shaped proton VDFs extend at least 400 km from the nucleus in the $+E$ hemisphere, as well as 100 km into the $-E$ hemisphere. This is a much larger region than previously thought (Moeslinger, Stenberg Wieser et al., 2023). The VDF in the central tail (P4) does not show a clearly dominating population. The observed particles seem to be a mix of several secondary populations. We also note that of all the sampling locations shown, the central tail region shows the largest diversity and spatial change in the shape of VDFs.

Close to the nucleus the alpha particles did not have enough time or space to evolve into complex VDFs (A3). Due to their larger inertia the alpha particle distributions are different from the proton distributions. The small anisotropy seen is consistent with observations (Moeslinger, Stenberg Wieser et al., 2023). When the alpha particles pass the electric field enhancement caused by the protons a few hundred kilometres below the nucleus, their velocity has a larger anti-sunward component compared to the protons. Hence the electric field does not form a potential barrier for them. Instead it accelerates them toward $-z$. At the alpha density enhancement (A2), the main population has gained about 200 eV in energy with respect to the upstream SW plasma. This energy is indirectly provided by the protons via the plasma boundary. The main alpha population downstream of the alpha density enhancement (A1) is a residual from the SW alphas entering through the $+E$ hemisphere that has not yet been deflected out of the y_0 plane. The secondary population must have gone through a full gyration before the observation point.

The high velocity part of the cometary ion VDFs (C1–C3) is a partial ring formed by the classical pickup process. The high speeds as well as the circular shape indicate that these ions were born far away from the observation point and have been accelerated in the undisturbed SW. Without additional electric field structures (apart from the undisturbed SW) the partial ring would start very close to $\mathbf{v} = (0,0,0)$. The offset of the ring structure is created by the inhomogeneous electric field around the nucleus. The lower velocity part of the distribution is formed by ions born closer to the observation point. Interpreting their more complex shapes is only possible with the help of the particle back-tracing results.

Anisotropic VDFs are inherently unstable. As the plasma evolves further away from the comet, the observed anisotropies in the VDFs will eventually relax back to Maxwellian-shaped distributions. The fully picked-up ring distributions of cometary ions will pitch-angle scatter into shells, which will eventually thermalize by energy diffusion (Coates et al., 1989). This process takes place over many gyrations and cannot be observed in our simulations due to the spatial limits of the tail downstream. The partial-ring-shaped VDFs of protons, and to a lesser extent alpha particles, can be interpreted as temperature anisotropies, or nongyrotropic distributions. Temperature anisotropies can result in the generation of mirror-mode waves which have been observed at comet 67P (Tello Fallau et al., 2023; Volwerk et al., 2016) and comet 1P/Halley (Russell et al., 1987; Schmid et al., 2014). However, all of these observations have associated the observed mirror modes with temperature anisotropies of cometary water group ions, not SW protons. Phase-space diffusion of nongyrotropic ion distributions has been studied for example, by Motschmann et al. (1997). Typical diffusion timescales, that is, the time until the nongyrotropic VDFs relax back to a Maxwellian equilibrium, are of the order of 10 gyroperiods, but some diffusion should already be visible after only one gyration. This may be one reason why the partial ring distributions are most pronounced close to the nucleus.

4.3. Particle Tracing

Particle tracing of the SW ions confirms that the observed particles close to the nucleus are on their first gyration from the upstream origin where they are initialized as isotropic SW in the simulation. The width (extent in the z direction) of the upstream origin area of SW protons is larger for P3 (close to the nucleus) than for the sampling locations P1 and P6. This is consistent with the wider spread in phase space of the main population at point P3. The energy of the particles at the observation point depends on their energy upstream, which is limited by the upstream velocity and temperatures, and how much they have moved with or against the electric field. The displacement in the electric field depends on the path of the individual particles and varies for particles of the main population for different observed velocities due to their different upstream origin. Ions from higher up along the z-axis have lost more energy if the overall deflection is toward $-z$. Since particles from the secondary populations

have passed through the highly inhomogeneous E-field region close to the nucleus their energies can change drastically compared to the main population. The origin of the main populations vary quite a lot between different sampling locations. Sampling locations at a higher z position also tend to have upstream origins from higher z. The upstream origin of the secondary location on the other hand seems to be within $0 < z < 500$ km for all particle trajectories analyzed. Therefore, the secondary populations observed in all the proton VDFs are created in a similar manner but then evolve into different regions. We note that at more negative z values than analyzed here secondary populations may still be created at the plasma boundary although the reflection geometry may be different.

The correlation between the level of deflection or gyration of the protons seen in the VDFs and the actual spatial gyration pattern is quite clear. It is possible to get a good approximation of the particle paths by taking the respective VDF and comparing it with the tracing patterns. Details are difficult to predict and still require the particle tracing for interpretation. The back-tracing also reveals the effects of the higher inertia of the alpha particles (Figure 7). The secondary population has been significantly deflected close to the nucleus where the fields are the strongest, but otherwise the deflection is more gradual. This was consistently observed in the back-tracing of several alpha particle VDFs, including the one shown here. From the upstream VDF probes (Figures 4–6, Panel b) we can see that the v_x component is much more important than the v_z component when it comes to correlating upstream location and upstream VDF shape.

For the cometary ions, particle gyration only seems to become relevant for ions with observed velocities above ≈150 km/s. The backtracing of these higher velocity ions shows that they are indeed born in the undisturbed SW at various distances from the observation location, with higher energetic particles originating further away from the observation point. For ions with velocities below 100−150 km/s the structure of the electric field is much more important for the resulting VDFs than any gyration motion. Any curvature in the low-velocity part of the VDFs (especially C3 in the $-v_x/+v_z$ quadrant) is not due to a gyration in the magnetic field but purely due to a structure in the electric field. The trajectories of these particles appear fairly straight and change in upstream origin location. If they were indeed due to a gyration in the magnetic field the curvature of the trajectories should be more pronounced. Steep gradients in the electric field result in sudden changes in the shape of the VDF. They do, however, not necessarily result in isolated populations. If such an isolated population is seen in the VDF it is a strong indicator that there are two unrelated paths from two separate regions in the cometosphere available for the cometary ions to take to the observation point.

5. Conclusions

In our simulations the plasma environment around a comet akin to comet 67P at larger heliocentric distances takes the shape of a highly asymmetric induced magnetosphere. Apart from the asymmetries in the $+E$ and $-E$ hemispheres often associated with such low-outgassing scenarios, we find that there is a formation of plasma boundaries in the $-E$ hemisphere. The $+E$ hemisphere lacks such clear boundaries, but provides an escape path for the cometary ions and is more susceptible to wave activity. Close to the nucleus strong electric and magnetic fields lead to highly anisotropic VDFs in the SW proton data, which resemble partial rings. Some protons of this anisotropic VDF split away from the bulk flow and are observed as secondary populations in both hemispheres. Similar distributions (partial rings with a secondary population) have previously been identified in Rosetta measurements of SW protons (Moeslinger, Stenberg Wieser et al., 2023). Solar wind alpha particles form VDFs with two populations further downstream, but they require a larger interaction region due to their higher inertia. Dynamic particle back-tracing aids in understanding the VDFs of all species, but is especially important for understanding the origin of cometary ions at a given location. The VDFs of cometary ions are mainly driven by electric field structures for velocities up to 100−150 km/s.

Appendix A: Global Magnetic Field Structures

Cross-sections of the spatial structure of electric and magnetic fields as well as ion densities and bulk flow along the magnetic field are shown in Figure A1. The magnetic field and the SW flow (especially protons) drapes around the obstacle of cometary ions, and a pile-up boundary is formed further downstream for larger distances from $y = 0$ km.

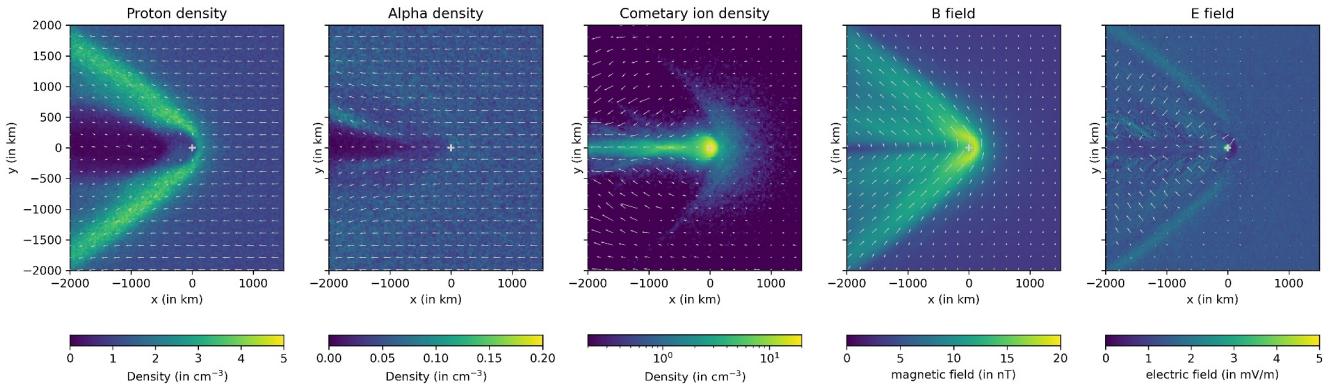

Figure A1. Ion densities and magnetic and electric fields in the $x-y$ plane, at z =0 km. The format is the same as Figure 1.

Appendix B: Electric Field in the SW Reference Frame

Figure B1 shows the electric field in different reference frames. The proton and alpha reference frames are derived from the local electric and magnetic field in the model reference frame ($\mathbf{B}(\mathbf{r})$ and $\mathbf{E}_{\text{model}}(\mathbf{r})$), and the local bulk velocity of the respective ion species ($\mathbf{v}_{\text{bulk}}(\mathbf{r})$) via Lorentz-transformation:

$$\mathbf{E}_{\text{ref}}(\mathbf{r}) = \mathbf{E}_{\text{model}}(\mathbf{r}) + \mathbf{v}_{\text{bulk}}(\mathbf{r}) \times \mathbf{B}(\mathbf{r}). \tag{B1}$$

This transformation was applied to every simulation cell.

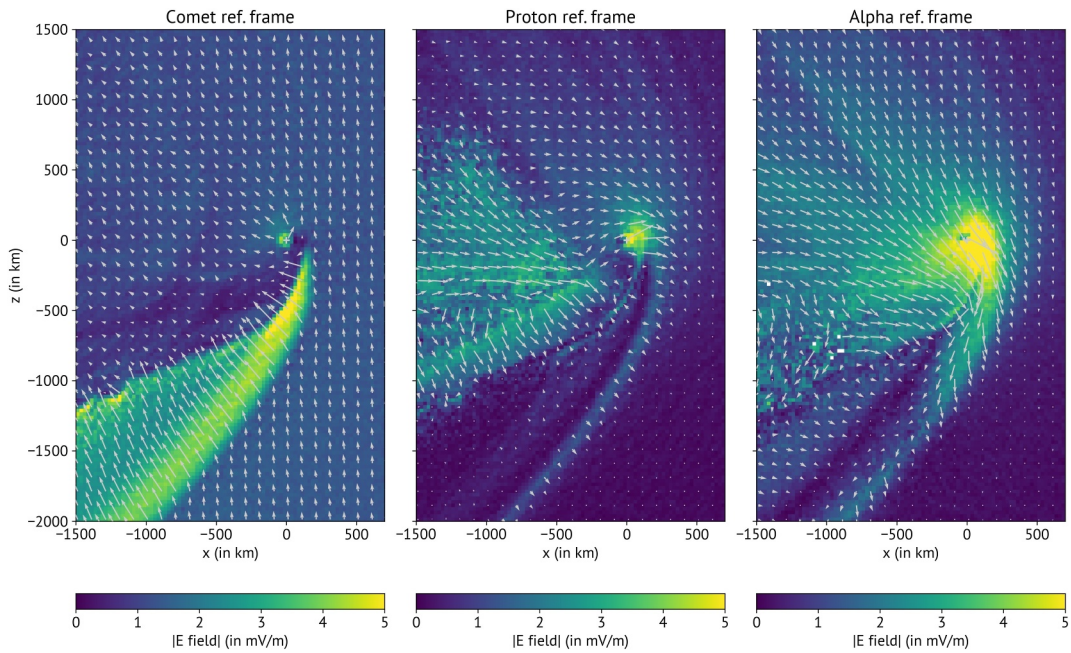

Figure B1. Electric field at $y = 0$ in different reference frames. Left: Model reference frame (same as Figure 1). Center: electric field transformed into the local proton reference frame. Right: electric field transformed into the local alpha particle reference frame.

Appendix C: VDF Locations

Figure C1 visualizes the location of the sampling locations individually for the three different species. The boxes are overlaid onto the ion density for the corresponding species.

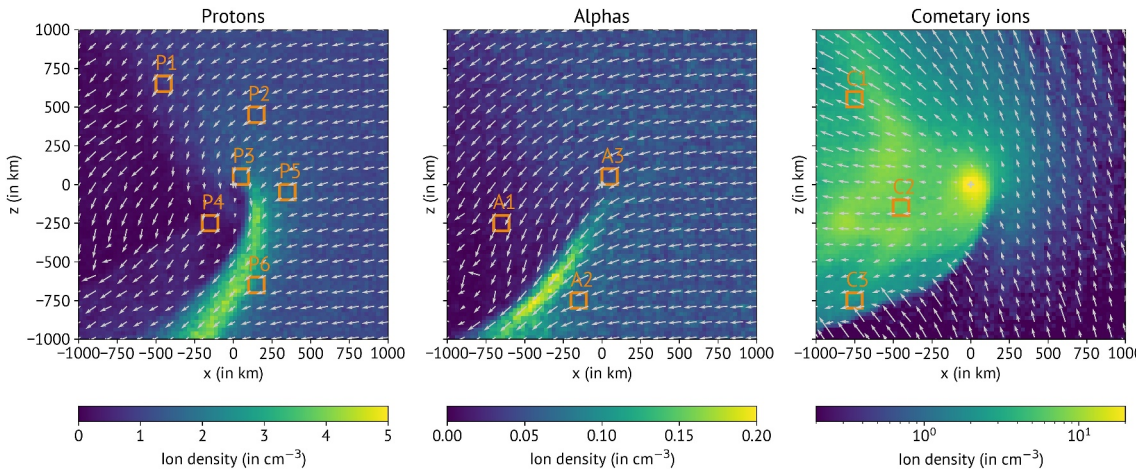

Figure C1. Location of the velocity distribution function sampling boxes for the different ion species. The background shows the ion density for the respective ion species (left: Protons, center: Alphas, right: cometary ions).

Data Availability Statement

Additional simulation results are included in the Supporting Information S1 of this paper. The code used for particle tracing has been made publicly available (see Moeslinger & Gunell, 2024). Data analysis was done using NumPy version 1.20.2 (Harris et al., 2020). Figures were made using Matplotlib (Caswell et al., 2021; Hunter, 2007).

Acknowledgments

The simulations were enabled by resources provided by the National Academic Infrastructure for Supercomputing in Sweden (NAISS) at High Performance Computing Center North (HPC2N) partially funded by the Swedish Research Council through Grant agreement no. 2022-06725. Work at the Swedish Institute of Space Physics in Kiruna (IRF) was funded by the Swedish National Space Agency (SNSA) Grant 132/19. Work at Umeå university was supported by SNSA Grant 2023-00208 (HG) and SNSA Grant 2022-00183 (SF).

References

Aizawa, S., Griton, L., Fatemi, S., Exner, W., Deca, J., Pantellini, F., et al. (2021). Cross-comparison of global simulation models applied to Mercury's dayside magnetosphere. *Planetary and Space Science*, *198*, 105176. https://doi.org/10.1016/j.pss.2021.105176

Alho, M., Jarvinen, R., Simon Wedlund, C., Nilsson, H., Kallio, E., & Pulkkinen, T. I. (2021). Remote sensing of cometary bow shocks: Modelled asymmetric outgassing and pickup ion observations. *Monthly Notices of the Royal Astronomical Society*, *506*(4), 4735–4749. https://doi.org/10.1093/mnras/stab1940

André, M., & Yau, A. (1997). Theories and observations of ion energization and outflow in the high latitude magnetosphere. *Space Science Reviews*, *80*(1), 27–48. https://doi.org/10.1023/A:1004921619885

Behar, E., Nilsson, H., Alho, M., Goetz, C., & Tsurutani, B. (2017). The birth and growth of a solar wind cavity around a comet - Rosetta observations. *Monthly Notices of the Royal Astronomical Society*, *469*(Suppl_2), S396–S403. https://doi.org/10.1093/mnras/stx1871

Behar, E., Nilsson, H., Wieser, G. S., Nemeth, Z., Broiles, T. W., & Richter, I. (2016). Mass loading at 67P/Churyumov-Gerasimenko: A case study. *Geophysical Research Letters*, *43*(4), 1411–1418. https://doi.org/10.1002/2015GL067436

Berčič, L., Behar, E., Nilsson, H., Nicolaou, G., Wieser, G. S., Wieser, M., & Goetz, C. (2018). Cometary ion dynamics observed in the close vicinity of comet 67P/Churyumov-Gerasimenko during the intermediate activity period. *Astronomy and Astrophysics*, *613*, A57. https://doi.org/10.1051/0004-6361/201732082

Biermann, L., Brosowski, B., & Schmidt, H. U. (1967). The interaction of the solar wind with a comet. *Solar Physics*, *1*(2), 254–284. https://doi.org/10.1007/BF00150860

Boris, J. P. (1970). Relativistic plasma simulation-optimization of a hybrid code. In *Proceedings: Fourth conference on numerical simulation of plasmas* (pp. 3–67). Naval Research Laboratory.

Broiles, T. W., Burch, J. L., Clark, G., Koenders, C., Behar, E., Goldstein, R., et al. (2015). Rosetta observations of solar wind interaction with the comet 67P/Churyumov-Gerasimenko. *Astronomy and Astrophysics*, *583*, A21. https://doi.org/10.1051/0004-6361/201526046

Caswell, T. A., Lee, M. D. A., de Andrade, E. S., Hunter, J., Hoffmann, T., Firing, E., & Ivanov, P. (2021). matplotlib/matplotlib: REL: v3.4.1 [Software]. https://doi.org/10.5281/zenodo.4649959

Coates, A. J., Johnstone, A. D., Wilken, B., Jockers, K., & Glassmeier, K.-H. (1989). Velocity space diffusion of pickup ions from the water group at comet Halley. *Journal of Geophysical Research: Space Physics*, *94*(A8), 9983–9993. https://doi.org/10.1029/ja094ia08p09983

Deca, J., Divin, A., Henri, P., Eriksson, A., Markidis, S., Olshevsky, V., & Horányi, M. (2017). Electron and ion dynamics of the solar wind interaction with a weakly outgassing comet. *Physical Review Letters*, *118*(20), 205101. https://doi.org/10.1103/PhysRevLett.118.205101

Divin, A., Deca, J., Eriksson, A., Henri, P., Lapenta, G., Olshevsky, V., & Markidis, S. (2020). A fully kinetic perspective of electron acceleration around a weakly outgassing comet. *The Astrophysical Journal Letters*, *889*(2), L33. https://doi.org/10.3847/2041-8213/ab6662

Dong, Y., Fang, X., Brain, D. A., McFadden, J. P., Halekas, J. S., Connerney, J. E., et al. (2015). Strong plume fluxes at Mars observed by MAVEN: An important planetary ion escape channel. *Geophysical Research Letters*, *42*(21), 8942–8950. https://doi.org/10.1002/2015GL065346

Dubinin, E., Fraenz, M., Zhang, T. L., Woch, J., Wei, Y., Fedorov, A., & Lundin, R. (2013). Plasma in the near Venus tail: Venus express observations. *Journal of Geophysical Research: Space Physics*, *118*(12), 7624–7634. https://doi.org/10.1002/2013JA019164

Edberg, N., Eriksson, A., Vigren, E., Nilsson, H., Gunell, H., Götz, C., et al. (2023). Scale size of cometary bow shocks. *Astronomy and Astrophysics*, *682*, A51. https://doi.org/10.1051/0004-6361/202346566

Fatemi, S., Poppe, A. R., Delory, G. T., & Farrell, W. M. (2017). AMITIS: A 3D GPU-based hybrid-PIC model for space and plasma physics. In *Journal of physics: Conference series* (Vol. 837). 012017, Institute of Physics Publishing. https://doi.org/10.1088/1742-6596/837/1/012017

Fatemi, S., Poppe, A. R., Vorburger, A., Lindkvist, J., & Hamrin, M. (2022). Ion dynamics at the magnetopause of Ganymede. *Journal of Geophysical Research: Space Physics*, *127*(1), e2021JA029863. https://doi.org/10.1029/2021JA029863

Galand, M., Héritier, K. L., Odelstad, E., Henri, P., Broiles, T. W., Allen, A. J., et al. (2016). Ionospheric plasma of comet 67P probed by Rosetta at 3 au from the Sun. *Monthly Notices of the Royal Astronomical Society*, *462*(Suppl 1), S331–S351. https://doi.org/10.1093/mnras/stw2891

Glassmeier, K.-H., Boehnhardt, H., Koschny, D., Kührt, E., & Richter, I. (2007). The Rosetta mission: Flying towards the origin of the solar system. *Space Science Reviews*, *128*(1–4), 1–21. https://doi.org/10.1007/s11214-006-9140-8

Goetz, C., Behar, E., Beth, A., Bodewits, D., Bromley, S., Burch, J., et al. (2022). The plasma environment of comet 67P/Churyumov-Gerasimenko. *Space Science Reviews*, *218*(8), 65. https://doi.org/10.1007/s11214-022-00931-1

Goetz, C., Gunell, H., Johansson, F., Llera, K., Nilsson, H., Glassmeier, K. H., & Taylor, M. G. (2021). Warm protons at comet 67P/Churyumov-Gerasimenko-implications for the infant bow shock. *Annales Geophysicae*, *39*(3), 379–396. https://doi.org/10.5194/angeo-39-379-2021

Gombosi, T. I., De Zeeuw, D. L., Häberli, R. M., & Powell, K. G. (1996). Three-dimensional multiscale MHD model of cometary plasma environments. *Journal of Geophysical Research: Space Physics*, *101*(A7), 15233–15253. https://doi.org/10.1029/96JA01075

Gombosi, T. I., Hansen, K. C., DeZeeuw, D. L., Combi, M. R., & Powell, K. G. (1997). MHD simulation of comets: The plasma environment of comet Hale-Bopp. *Earth, Moon, and Planets*, *79*(1), 179–207. https://doi.org/10.1023/A:1006289418660

Graham, D. B., Khotyaintsev, Y. V., Dimmock, A. P., Lalti, A., Boldú, J. J., Tigik, S. F., & Fuselier, S. A. (2024). Ion dynamics across a low mach number bow shock. *Journal of Geophysical Research: Space Physics*, *129*(4), e2023JA032296. https://doi.org/10.1029/2023JA032296

Gulkis, S., Allen, M., Von Allmen, P., Beaudin, G., Biver, N., Bockelée-Morvan, D., et al. (2015). Subsurface properties and early activity of comet 67P/Churyumov-Gerasimenko. *Science*, *347*(6220), aaa0709. https://doi.org/10.1126/science.aaa0709

Gunell, H., & Goetz, C. (2023). Particle-in-cell modelling of comet 67P/Churyumov-Gerasimenko: Spatial structures of densities and electric fields. *Astronomy and Astrophysics*, *674*, A65. https://doi.org/10.1051/0004-6361/202245197

Gunell, H., Goetz, C., & Fatemi, S. (2024). Impact of radial interplanetary magnetic fields on the inner coma of comet 67P/Churyumov-Gerasimenko - Hybrid simulations of the plasma environment. *Astronomy and Astrophysics*, *682*, A62. https://doi.org/10.1051/0004-6361/202348186

Gunell, H., Goetz, C., Simon Wedlund, C., Lindkvist, J., Hamrin, M., Nilsson, H., et al. (2018). The infant bow shock: A new Frontier at a weak activity comet. *Astronomy & Astrophysics*, *619*, L2. https://doi.org/10.1051/0004-6361/201834225

Gunell, H., Mann, I., Wedlund, C. S., Kallio, E., Alho, M., Nilsson, H., et al. (2015). Acceleration of ions and nano dust at a comet in the solar wind. *Planetary and Space Science*, *119*, 13–23. https://doi.org/10.1016/j.pss.2015.08.019

Hansen, K. C., Altwegg, K., Berthelier, J. J., Bieler, A., Biver, N., Bockelée-Morvan, D., et al. (2016). Evolution of water production of 67P/Churyumov-Gerasimenko: An empirical model and a multi-instrument study. *Monthly Notices of the Royal Astronomical Society*, *462*, S491–S506. https://doi.org/10.1093/mnras/stw2413

Harris, C. R., Millman, K. J., van der Walt, S. J., Gommers, R., Virtanen, P., Cournapeau, D., et al. (2020). Array programming with NumPy. *Nature*, *585*(7825), 357–362. https://doi.org/10.1038/s41586-020-2649-2

Haser, L. (1957). Distribution d'intensité dans la tête d'une comète. *Bulletin de la Société Royale des Sciences de Liège*, *43*(1), 740–750. https://doi.org/10.3406/barb.1957.68714

Heritier, K. L., Galand, M., Henri, P., Johansson, F. L., Beth, A., Eriksson, A. I., et al. (2018). Plasma source and loss at comet 67P during the Rosetta mission. *Astronomy and Astrophysics*, *618*, A77. https://doi.org/10.1051/0004-6361/201832881

Heritier, K. L., Henri, P., Vallières, X., Galand, M., Odelstad, E., Eriksson, A. I., et al. (2017). Vertical structure of the near-surface expanding ionosphere of comet 67P probed by Rosetta. *Monthly Notices of the Royal Astronomical Society*, *469*(Suppl_2), S118–S129. https://doi.org/10.1093/mnras/stx1459

Holmström, M., Fatemi, S., Futaana, Y., & Nilsson, H. (2012). The interaction between the moon and the solar wind. *Earth Planets and Space*, *64*(2), 237–245. https://doi.org/10.5047/eps.2011.06.040

Huang, Z., Tóth, G., Gombosi, T. I., Jia, X., Rubin, M., Fougere, N., et al. (2016). Four-fluid MHD simulations of the plasma and neutral gas environment of comet 67P/Churyumov-Gerasimenko near perihelion. *Journal of Geophysical Research: Space Physics*, *121*(5), 4247–4268. https://doi.org/10.1002/2015JA022333

Hunter, J. D. (2007). Matplotlib: A 2d graphics environment. *Computing in Science and Engineering*, *9*(3), 90–95. https://doi.org/10.1109/MCSE.2007.55

Jasinski, J. M., Regoli, L. H., Cassidy, T. A., Dewey, R. M., Raines, J. M., Slavin, J. A., et al. (2020). A transient enhancement of Mercury's exosphere at extremely high altitudes inferred from pickup ions. *Nature Communications*, *11*(1), 4350. https://doi.org/10.1038/s41467-020-18220-2

Jones, G. H., Snodgrass, C., Tubiana, C., Küppers, M., Kawakita, H., Lara, L. M., et al. (2024). The comet interceptor mission. *Space Science Reviews*, *220*(1), 9. https://doi.org/10.1007/s11214-023-01035-0

Koenders, C., Glassmeier, K.-H., Richter, I., Ranocha, H., & Motschmann, U. (2015). Dynamical features and spatial structures of the plasma interaction region of 67P/Churyumov–Gerasimenko and the solar wind. *Planetary and Space Science*, *105*, 101–116. https://doi.org/10.1016/j.pss.2014.11.014

Koenders, C., Perschke, C., Goetz, C., Richter, I., Motschmann, U., & Glassmeier, K. H. (2016). Low-frequency waves at comet 67P/Churyumov-Gerasimenko: Observations compared to numerical simulations. *Astronomy and Astrophysics*, *594*, A66. https://doi.org/10.1051/0004-6361/201628803

Ledvina, S. A., Ma, Y.-J., & Kallio, E. (2008). Modeling and simulating flowing plasmas and related phenomena. *Space Science Reviews*, *139*(1–4), 143–189. https://doi.org/10.1007/s11214-008-9384-6

Lee, S., Von Allmen, P., Allen, M., Beaudin, G., Biver, N., Bockelée-Morvan, D., et al. (2015). Spatial and diurnal variation of water outgassing on comet 67P/Churyumov-Gerasimenko observed from Rosetta/MIRO in August 2014. *Astronomy and Astrophysics*, *583*, A5. https://doi.org/10.1051/0004-6361/201526155

Madanian, H., Schwartz, S. J., Halekas, J. S., & Wilson, L. B. (2020). Nonstationary quasiperpendicular shock and ion reflection at Mars. *Geophysical Research Letters*, *47*(11). https://doi.org/10.1029/2020GL088309

Mandt, K. E., Eriksson, A., Edberg, N. J. T., Koenders, C., Broiles, T., Fuselier, S. A., et al. (2016). RPC observation of the development and evolution of plasma interaction boundaries at 67P/Churyumov-Gerasimenko. *Monthly Notices of the Royal Astronomical Society*, *462*(Suppl 1), S9–S22. https://doi.org/10.1093/mnras/stw1736

Moeslinger, A., & Gunell, H. (2024). Particle tracing code [Software]. *Zenodo*. https://doi.org/10.5281/zenodo.10973547

Moeslinger, A., Nilsson, H., Stenberg Wieser, G., Gunell, H., & Goetz, C. (2023). Indirect observations of electric fields at comet 67P. *Journal of Geophysical Research: Space Physics*, *128*(9), e2023JA031746. https://doi.org/10.1029/2023JA031746

Moeslinger, A., Stenberg Wieser, G., Nilsson, H., Gunell, H., Williamson, H. N., Llera, K., & Richter, I. (2023). Solar wind protons forming partial ring distributions at comet 67P. *Journal of Geophysical Research: Space Physics*, *128*. https://doi.org/10.1029/2022JA031082

Motschmann, U., Kafemann, H., & Scholer, M. (1997). Nongyrotropy in magnetoplasmas: Simulation of wave excitation and phase-space diffusion. *Annales Geophysicae*, *15*(6), 603–613. https://doi.org/10.1007/s00585-997-0603-3

Neubauer, F. M., Glassmeier, K. H., Pohl, M., Raeder, J., Acuna, M. H., Burlaga, L. F., et al. (1986). First results from the giotto magnetometer experiment at comet Halley. *Nature*, *321*(6067s), 352–355. https://doi.org/10.1038/321352a0

Neugebauer, M., Lazarus, A., Balsiger, H., Fuselier, S., Neubauer, F., & Rosenbauer, H. (1989). The velocity distributions of cometary protons picked up by the solar wind. *Journal of Geophysical Research*, *94*(A5), 5227–5239. https://doi.org/10.1029/JA094iA05p05227

Nilsson, H., Gunell, H., Karlsson, T., Brenning, N., Henri, P., Goetz, C., et al. (2018). Size of a plasma cloud matters: The polarisation electric field of a small-scale comet ionosphere. *Astronomy and Astrophysics*, *616*, A50. https://doi.org/10.1051/0004-6361/201833199

Nilsson, H., Wieser, G. S., Behar, E., Gunell, H., Wieser, M., Galand, M., et al. (2017). Evolution of the ion environment of comet 67P during the rosetta mission as seen by RPC-ICA. *Monthly Notices of the Royal Astronomical Society*, *469*(Suppl_2), S252–S261. https://doi.org/10.1093/mnras/stx1491

Rubin, M., Combi, M. R., Daldorff, L. K. S., Gombosi, T. I., Hansen, K. C., Shou, Y., et al. (2014). Comet 1P/Halley multifluid MHD model for the *Giotto* fly-by. *The Astrophysical Journal*, *781*(2), 86. https://doi.org/10.1088/0004-637X/781/2/86

Russell, C. T., Riedler, W., Schwingenschuh, K., & Yeroshenko, Y. (1987). Mirror instability in the magnetosphere of comet Halley. *Geophysical Research Letters*, *14*(6), 644–647. https://doi.org/10.1029/GL014i006p00644

Schmid, D., Volwerk, M., Plaschke, F., Vörös, Z., Zhang, T. L., Baumjohann, W., & Narita, Y. (2014). Mirror mode structures near Venus and Comet P/Halley. *Annales Geophysicae*, *32*(6), 651–657. https://doi.org/10.5194/angeo-32-651-2014

Sckopke, N., Gosling, J. T., Russell, C. T., & Bame, S. J. (1983). Evolution of ion distributions across the nearly perpendicular bow shock: Specularly and non-specularly reflected-gyrating ions. *Journal of Geophysical Research*, *88*(A8), 6121–6136. https://doi.org/10.1029/JA088iA08p06121

Sun, W., Dewey, R. M., Jia, X., Raines, J. M., Slavin, J. A., Chen, Y., et al. (2024). Messenger observations of mercury's planetary ion escape rates and their dependence on true anomaly angle. *Geophysical Research Letters*, *51*(13), e2023GL107689. https://doi.org/10.1029/2023GL107689

Taylor, M. G. G. T., Altobelli, N., Buratti, B. J., & Choukroun, M. (2017). The Rosetta mission orbiter science overview: The comet phase. *Philosophical Transactions of the Royal Society of London A: Mathematical, Physical and Engineering Sciences*, *375*(2097), 20160262. https://doi.org/10.1098/rsta.2016.0262

Tello Fallau, A., Goetz, C., Simon Wedlund, C., Volwerk, M., & Moeslinger, A. (2023). Revisiting mirror modes in the plasma environment of comet 67P/Churyumov–Gerasimenko. *Annales Geophysicae*, *41*(2), 569–587. https://doi.org/10.5194/angeo-41-569-2023

Volwerk, M., Richter, I., Tsurutani, B., Götz, C., Altwegg, K., Broiles, T., et al. (2016). Mass-loading, pile-up, and mirror-mode waves at comet 67P/Churyumov-Gerasimenko. *Annales Geophysicae*, *34*(1), 1–15. https://doi.org/10.5194/angeo-34-1-2016

Wang, X.-D., Fatemi, S., Holmström, M., Nilsson, H., Futaana, Y., & Barabash, S. (2023). Martian global current systems and related solar wind energy transfer: Hybrid simulation under nominal conditions. *Monthly Notices of the Royal Astronomical Society*, *527*(4), 12232–12242. https://doi.org/10.1093/mnras/stad3486

Williamson, H. N., Nilsson, H., Stenberg Wieser, G., A. Moeslinger, A., & Goetz, C. (2022). Development of a cometosheath at comet 67P/Churyumov-Gerasimenko - a case study comparison of Rosetta observations. *A&*, *660*, A103. https://doi.org/10.1051/0004-6361/202142461